Multiplexed 3D Analysis of Immune States and Niches in Human Tissue

Clarence Yapp[1,2,*], Ajit J. Nirmal[1,2,3,*], Felix Zhou[4], Zoltan Maliga[1], Juliann B. Tefft[1,2], Paula Montero Llopis[5], George F. Murphy[6], Christine G. Lian[6], Gaudenz Danuser[4], Sandro Santagata[1,2,6,7] and Peter K. Sorger[1,2,7,†]

Human Tumour Atlas Network

[1]Laboratory of Systems Pharmacology, Harvard Medical School, Boston, MA, 02115, USA.

[2]Ludwig Centre at Harvard, Harvard Medical School, Boston, MA, 02115, USA.

[3]Department of Dermatology, Brigham and Women's Hospital, Harvard Medical School, Boston, MA, 02115, USA.

[4]Lyda Hill Department of Bioinformatics, UT Southwestern Medical Center, Dallas, TX, 75390, USA.

[5]Microscopy Resources on the North Quad (MicRoN), Harvard Medical School, Boston, MA 02115, USA.

[6]Department of Pathology, Brigham and Women's Hospital, Harvard Medical School, Boston, MA, 02115, USA.

[7]Department of Systems Biology, Harvard Medical School, 200 Longwood Avenue, Boston, MA 02115, USA.

*Authors contributed equally

†Corresponding Author; peter_sorger@hms.harvard.edu

ORCID:

Clarence Yapp - 0000-0003-1144-5710

Ajit J. Nirmal - 0000-0003-4139-0618

Felix Zhou- 0000-0003-4463-1165

Zoltan Maliga- 0000-0003-4209-7253

Paula Montero Llopis- 0000-0002-5983-2296

Juliann B. Tefft- 0000-0002-8826-665X

George Murphy- 0000-0001-9362-5146

Christine Lian- 0000-0003-4626-1612

Gaudenz Danuser- 0000-0001-8583-2014

Sandro Santagata - 0000-0002-7528-9668

Peter K Sorger - 0000-0002-3364-1838

SUMMARY

Tissue homeostasis and the emergence of disease are controlled by changes in the proportions of resident and recruited cells, their organization into cellular neighbourhoods, and their interactions with acellular tissue components. Highly multiplexed tissue profiling (spatial omics)[1] makes it possible to study this microenvironment *in situ*, usually in 4-5 micron thick sections (the standard histopathology format)[2]. Microscopy-based tissue profiling is commonly performed at a resolution sufficient to determine cell types but not to detect subtle morphological features associated with cytoskeletal reorganisation, juxtracrine signalling, or membrane trafficking[3]. Here we describe a high-resolution 3D imaging approach able to characterize a wide variety of organelles and structures at sub-micron scale while simultaneously quantifying millimetre-scale spatial features. This approach combines cyclic immunofluorescence (CyCIF) imaging[4] of over 50 markers with confocal microscopy of archival human tissue thick enough (30-40 microns) to fully encompass two or more layers of intact cells. 3D imaging of entire cell volumes substantially improves the accuracy of cell phenotyping and allows cell proximity to be scored using plasma membrane apposition, not just nuclear position. In pre-invasive melanoma *in situ*[5], precise phenotyping shows that adjacent melanocytic cells are plastic in state and participate in tightly localised niches of interferon signalling near sites of initial invasion into the underlying dermis. In this and metastatic melanoma, mature and precursor T cells engage in an unexpectedly diverse array of juxtracrine and membrane-membrane interactions as well as looser "neighbourhood" associations[6] whose morphologies reveal functional states. These data provide new insight into the transitions occurring during early tumour formation and immunoediting and demonstrate the potential for phenotyping of tissues at a level of detail previously restricted to cultured cells and organoids.

MAIN

Since the first cultured cell lines, analysis of cell and organelle morphology has informed our understanding of cell mechanics, cell-cell signalling, and disease[7]. Morphology also plays a central role in conventional histopathological diagnosis using haematoxylin and eosin (H&E) stained tissue sections. High-plex spatial profiling extends such approaches by quantifying diverse molecular and phenotypic features in a preserved tissue environment. In spatial transcriptomics[8], the ability to discriminate cells depends primarily on the number of genes measured, but in imaging with antibodies, both the number of antigens and their precise intracellular distributions determine information content[9]. Nonetheless, almost all contemporary high-plex image-based profiling emphasizes relatively low resolution 2D imaging (0.6 to 2.0 µm lateral resolution) of conventional 5 µm thick tissue sections to increase the speed and convenience of data acquisition.

To study the impact of tissue thickness and image resolution on accurate cell type assessment, formaldehyde-fixed paraffin-embedded (FFPE) tissue blocks were sectioned at thicknesses ranging from 5 to 40 µm (processing thicker sections was infeasible with current techniques) and subjected to 3D CyCIF imaging using a multi-spectral Zeiss LSM980 laser scanning confocal microscope. This revealed that, in conventional 5 µm sections, nearly all nuclei (>90%) were incomplete along the Z (optical) axis whereas, in 30-40 µm sections, 60-80% of nuclear envelopes were complete along all three axes (**Fig. 1a; Supplementary Video 1**). In many areas of a thick specimen, multiple layers of intact nuclei were visible (**Fig. 1a-c)**.

To study the impact of thick section imaging on cell phenotyping, volumetric reconstruction was performed on small communities of cells using Imaris® (RRID:SCR_007370) software. **Figure 1c** shows one community, comprising a dendritic cell (*D*) and two T cells (*T1, T2*), from a 54-plex CyCIF image of a 35 µm thick section of invasive (vertical growth phase; VGP) primary melanoma; the cells spanned ~25 µm along the optical axis (Z; upper image) and a similar distance in the plane of the specimen (X,Y; lower image). In these cells, surface antigens commonly used to subtype immune cells had non-uniform distributions and the T-cell activation and exhaustion markers PD-1 and LAG3 were polarized (see **Supplementary Table 1** for protein nomenclature). When we created sequential synthetic 5 µm serial 'sections' (2D maximum intensity projections; labelled I to V) along the Z axis, inferred cell types varied with the section and was often incorrect (**Fig. 1d**). Using synthetic section III as an example, *D* would be incorrectly scored as negative for the inflammatory marker MX1 due to its polarized distribution and positive for LAG3 due to overlap with cell *T1*, while true positive staining from *T1* and *T2* (CD8 and LAG3) would be scored as background because the corresponding nuclei were largely absent from the section (cell segmentation methods rely on nuclei). Thus, accurate phenotyping of these three immune cells requires imaging whole cells to account for non-uniform protein distributions in cells and their overlap in Z.

The ~5 µm projections of high-resolution images in **Figure 1d** do not correctly represent what would be seen in a conventional lower resolution 2D slide scanner. This arises because the volume of emitted photons (the point spread function) collected by a confocal microscope relative to a widefield scanner (with 0.5 Numerical Aperture objective) is ~3 fold smaller in X,Y and 5-fold smaller in Z; emitted light from out-of-focus planes is also lower. These effects are approximated in the lower right panel of **Figure 1d** ('ψ widefield") and show that punctate signals commonly representing intracellular organelles, condensates, and other localized protein complexes cannot be readily distinguished from each other and from background noise at lower resolution (see **Extended Data Fig. 1a** for individual channel views).

We then collected 11 datasets (**Supplementary Table 2**) from five tissue types (representing normal, cancerous, and pre-cancerous tissues) using thick section 3D high-plex CyCIF imaging with 140 x 140 x 280 nm voxels (~1,000,000 voxels per cell). Datasets averaged ~500 gigabyte per mm^2

of tissue (see **Supplementary Figs. 1-11** for illustrative results of all tissues). Antibody specificity was confirmed on 5 µm sections of the same specimens, as previously described[10]. Extracellular matrix (collagen) was imaged with Second Harmonic Generation by Fluorescence Lifetime Imaging Microscopy (SHG; **Fig. 1e**). A newly developed 3D segmentation algorithm was used to identify single cells, generate UMAP embeddings, and distinguish among major immune and tumour cell types (**Extended Data Fig. 1b**). Because methods for systematic assessment of 3D high-plex morphologies do not yet exist, we relied on visual analysis; key findings were then confirmed computationally. For simplicity, the current manuscript focuses on three datasets in one disease: (i) a pre-invasive cutaneous melanoma in situ (MIS), (ii) a VGP primary melanoma from the same patient (**Fig. 1e**, **Extended Data Fig. 1c-d**), and (iii) a metastatic melanoma to the skin from a different patient. We have organized the description of these specimens around key topics in spatial biology: analysis of cell and organelle morphology, the microanatomy of cell clusters and structures (e.g. blood vessels), cell shape, tumour and immune cell lineages, and cell-cell interactions (proximity analysis). Throughout, we highlight protein distributions that have functional significance based on historical studies with cultured cells and organoids.

Across all specimens, cells were densely packed except in areas where blood vessels or ECM filled the voids (**Fig. 1f; Supplementary Video 3**). In the MIS, for example, nuclei averaged 5.0 µm in diameter (mean 7.2 µm ± 2.3 µm SD for melanocytes and 4.9 µm ± 2.8 µm for immune cells). Cells averaged 13 µm ± 4.3 µm along the major axis, 6.1 µm ± 1.9 µm along the minor axis (consistent with recent and historical estimates)[11]. Thus, the depth of the cytoplasmic compartment, scored as the distance from the plasma membrane to the nuclear lamina, was often 1 to 6 µm and the membranes of neighbouring cells were located only 1 to 1.5 µm apart (**Fig. 1g,h)**.

Some cells had highly extended cell bodies and cytoplasmic processes. For example, in **Figure 1i,** three $CD8^+$ T cells from metastatic melanoma had multiple filipodia extending 5-10 µm from the cell body. A dendritic cell had 20-30 µm filopodia and membrane ruffles in contact with multiple $CD8^+$ $PD1^+$ effector T cells; these specialized filopodia (dendrites) enable a switch from antigen sampling to antigen presentation during T cell priming[12] (**Fig. 1j, Extended Data Fig. 1e,f,**). Langerhans cells, specialized dendritic cells in skin, also had many membrane extensions, with branches extending 30-50 µm across multiple Z planes (**Fig. 1k**)**.** 3D imaging was essential to identify these morphologies, and to distinguish changes in cell shape from changes in orientation: 2D views of VGP melanoma suggested that round cells were more common in the tumour centre and elongated cells at the tumour margin. In 3D this was seen to be an artefact of differences in orientation: cells in the centre were more likely to be viewed end-on whereas those in the margin were rotated ~90° (**Extended Data Fig. 1g-i).** Theoretical and experimental studies of cell migration have demonstrated a dependency on both the intrinsic properties of cells and their packing[13]. Accurate 3D representations of tissues and their constituents will be useful in such studies. Moreover, tight

cell packing, extended processes, and overlap along the Z-axis explain why accurate single-cell segmentation of 2D images and spatial transcriptomic profiles[14] is inherently challenging**.**

Organelle and cell surface morphologies

High-plex imaging of whole immune and tumour cells in 3D made it possible to identify a wide variety of discrete intracellular and plasma-membrane structures (**Fig. 2a)** including lineage-associated differences in nuclear lamina (e.g., a multi-lobed – hyper-segmented – nucleus in neutrophils; **Fig. 2b**), microtubule organising centres (**Fig. 2c**), peroxisomes (based on catalase staining), secretory granules and/or ER (lysozyme C in neutrophils and granzyme B in T cells)**,** DNA damage foci (γH2AX), mitochondria (COX IV), and biomolecular condensates (MX1[15]; **Fig. 2d-h, Extended Data Fig. 2a**). Galleries of single cells identified broadly distributed and cell-type specific features (e.g., catalase foci in dendritic cells and γH2AX foci in keratinocytes and myeloid cells), enabling deep phenotyping of cell lineage and state.

Proteins used for lineage analysis exhibited a variety of distributions that proved helpful in subtyping. Some were distributed throughout the plasma membrane, for example the myeloid cell integrin CD11c, skin-homing T cell integrin CD103, and MHCII receptor (in tumour and antigen presenting cells). Others were found in discontinuous islands (CD4 and CD8 in T cells) or puncta (the immune checkpoint protein LAG3; **Fig. 2i-l**). The distributions of some proteins provided information on activity or cell state. For example, newly synthesized LAG3 localizes to endosomes but can rapidly translocate to the plasma membrane where it is activated by binding to MHC class II[16] on the membranes of apposed cells. Across specimens, we found 1-20 LAG3 puncta per cell, both inside cells and at the plasma membrane (**Extended Data Fig. 2b**). Granzyme B (GZMB) staining was diffuse and globular in CD4 T cells and punctate in CD8 T cells, consistent with localization to cytoplasmic granules. GZMB mediates the cytotoxic activity of T and NK cells and globular GZMB can be used to identify activated memory CD4 T cells (**Fig. 2m, Extended Data Fig. 2c; Supplementary Video 4**)[17].

Functional interactions among cells could be inferred from changes in the distributions of cell surface proteins. For example, the immune checkpoint receptor PD1 and its transmembrane ligand PD-L1 varied from relatively uniform in the membrane to punctate (**Fig. 2n-o; Extended Data Fig. 2d-f**), with the latter morphology most evident when $PD1^+$ T cells were in contact with PDL1 expressing cells (primarily dendritic cells).[18] In some cases, many PD1 and PDL1 puncta were visible across an extended domain of membrane apposition (e.g., 13 foci over 40 μm^2 in **Fig. 2o**), in an arrangement consistent with formation of multiple juxtracrine signalling complexes. Multiple distinctive membrane structures were commonly visible in a single cell; for example, filipodia from a CD8 T cell contacting a tumour cell while PD1 was bound to PDL1 from a neighbouring dendritic cell (**Fig. 2p-r**, **Extended Data Fig. g-i**). In a different multicellular community, filipodia from a CD8 T cell contacted a CD4 T helper cell (**Fig. 2s;** inset, **Extended Data Fig. 2j)**, which in turn contacted

another CD8 T cell that was in contact with both a tumour cell and a dendritic cell; GZMB in this T cell was polarized toward the tumour cell **(Fig. 2t**; green arrowhead**)** and PD1-PDL1 complexes had also formed (blue arrowhead). Thus, morphologically distinguishable interactions involving a variety of intracellular and cell surface proteins provide insight into complex patterns of T-cell regulation and activation.

Tumour microarchitecture

Thick section 3D imaging made it possible to dissect components of the tissue microarchitecture such as a 100 µm-long dermal blood vessel (venule) in the MIS (**Fig. 3a; Supplementary Video 2)**. In this vessel, ~10 vimentin and beta-catenin-positive endothelial cells formed a tube enclosing erythrocytes (labelled "6") and a neutrophil (4). At the distal end, a helper T (2) and dendritic (1) cell were visible where the vessel appeared to branch. Most remarkable was a B cell (5) with a low sphericity (value of ~0.35) flattened against the vessel wall, a morphology consistent with trans-endothelial migration (diapedesis) of immune cells from vessels into tissues[19]. These features were not evident in virtual 5 µm-thick sections (**Extended Data Fig. 3a**). Elsewhere in the dermis, another B cell had its nucleus traversing a vessel wall while its cell body remained inside the vessel while in in metastatic melanoma a T cell was suspended within a vessel (**Extended Data Fig. 3b-c**). In the MIS as a whole, we found that B cells were the type of cell most likely to associate with collagen fibres in the dermis[20,21] (**Fig. 3b, c)**; they were often (n = 11 of 14 in the MIS) stretched into irregular shapes (this was not a feature of all B cells and those found in the stroma were often round; **Extended Data Fig. 3d**). Functions have only recently been ascribed to B cells in the skin and our images provide direct evidence of B cell recruitment from the vasculature into the dermis, followed by collagen binding, at densities consistent with other reports[22].

Cell shape and motility

Cell shape and motility are regulated by the actomyosin cytoskeleton which was most prominent in dendritic and T cells (~2-fold more actin overall than melanocytic cells and 3-fold more than in keratinocytes; **Fig. 3d**). This manifested itself as a dense network of plasma membrane-proximal cortical actin (**Fig. 3e,** panel 1&2**; Extended Data Fig. 4a**). Tumour cells had indistinct actin networks but frequent plasma membrane-localised puncta (0.45 puncta per cell in the interior vs. 0.06 per cell at the tumour margin; panel 3), which may represent invadopodia[23]. Nuclear actin rods were another atypical actin morphology, found in ~14% of melanocytic cells in MIS (**Extended Data Fig. 4b-d)**, and have previously been associated with a stress response[24]. This may reflect contact between rod-positive cells and one or two activated $CD8^+$ $PD1^+$ cytotoxic T cells.

Melanocytes (and epithelial cells) form lateral adherens junctions (mediated by E-cadherin) that connect to the actin cytoskeleton through linker proteins such as beta-catenin; these junctions play a key role in melanocyte differentiation and oncogenesis[25]. Adherens junctions are often under

tension due to opposing contractile forces in adjacent cells. Phosphorylation of myosin light chain 2 (pMLC2) regulates this tension by promoting actomyosin contractility. In VGP melanoma, E-cadherin staining was greatest in the centre of the tumour (**Fig. 3f**) and was positively correlated with levels of β-catenin (panel 4), but inversely correlated with pMLC2 staining at the tumour margin (panel 5). Single tumour cells midway between the margin and centre exhibited alternative staining for pMLC2 and E-cadherin (panel 6). This pattern likely reflects lower adhesion and greater tension at the tumour margin and more adhesion and lower tension at the tumour core[26], perhaps in response to an immune cell-proximate inflammatory environment[27] (which manifests itself as MHC-II upregulation in tumour cells at the margin; **Fig. 3f**). Such an arrangement is expected to promote invasion of the underlying dermis. Infrequent pMLC2 positive cells in the tumour centre were found be myeloid and T cells; these cells had abundant cortical actin and extended cytoplasmic processes (**Fig. 3e;** panels 1&2). We propose that these represent immune cells actively migrating into the tumour core.

Tumour lineage plasticity

Although the genetics of later stage melanoma are well characterized[28], mechanisms of melanoma initiation remain elusive[29]. A handful of studies have identified oncogenic mutations (such as BRAF, NRAS, NF1)[28] and reductions in the DNA epigenetic marker, 5-Hydroxymethylcytosine (5hmc)[30], in melanoma precursors suggesting a role for both genetic and epigenetic changes. Currently, the presence of melanoma precursor fields[5] and MIS is scored by changes in the morphologies, numbers, and positions of melanocytic cells in H&E images[31] (expression of protein markers such as PRAME[32] is also used in diagnosis). In the MIS region, most melanocytic cells were located at the dermal-epidermal junction (DEJ), interacted with keratinocytes, and retained a dendritic morphology (promoting transfer of UV-protective melanin; **Fig. 4a**). Also present were pagetoid melanocytic cells that lacked dendrites and had a rounded, ameboid morphology (cytological atypia), which was most obvious among cells that had migrated towards the top of the epidermis (**Fig. 4b-h)**. Pagetoid spread by single and small groups of cells is a hallmark of oncogenic transformation[33]. Nonetheless, the MIS and underlying dermis were not highly proliferative, with only 1% of cells (n = 110) positive for the $Ki67^+$ proliferation marker. Among $Ki67^+$ cells, 34% were T cells while the remainder consisted of monocytes (28%) and endothelial cells (2.7%); only a single melanocytic cell was $Ki67^+$. By contrast, in the invasive VGP melanoma domain from the same specimen, 11% of all cells were $Ki67^+$ with melanoma tumour cells the most proliferative (45% $Ki67^+$), followed by monocytes (44%). Thus, the MIS had the hallmarks of early oncogenic transformation and migration, but limited cell division (proliferation is known to vary among MIS specimens)[34].

We scored individual melanocytic cells (n=875) in the MIS for expression of six markers of melanocyte lineage and transformation, including 5hmc, PRAME, MART1 (a melanocyte cell surface protein used clinically)[35], SOX9, SOX10, and MITF (transcription factors associated with

differentiation). 3D imaging made it possible to unambiguously score combinations of nuclear and cell surface markers at a single cell level and revealed that the six markers we scored were present in all 63 possible combinations, without evidence of significant spatial correlation (**Fig. 4i-s**), Cells undergoing pagetoid spread also expressed many different combinations of lineage markers (**Fig. 4c-h**) and transcription factors (**Fig. 4m,n**). Additionally, in the case of SOX9 and SOX10, there was clear evidence of a graded transition between states (**Fig. 4t**). However, we did not detect expression of NGFR (CD271), a marker of melanoma initiating "stem" cells[36] in the MIS or the VGP melanoma (as a control, we confirmed positive NGFR staining in parallel thin-sections of a separate case of metastatic melanoma). Moreover, in the MIS we did not detect any association between cell-intrinsic markers and melanocyte morphology or other features such as nuclear actin rods. These data imply that melanocytic cells with features of early malignant transformation are subject to frequent changes in cell state (phenotypic plasticity) rather than progressive evolution from a single transformed or progenitor (stem-like) cell, as proposed for advanced invasive melanoma.

Inflammatory neighbourhoods

We also observed changes in immunogenic state affecting cellular neighbourhoods. For example, the MIS contained three spatially restricted domains in which the levels or distributions of IRF1, MX1, and MHC-I revealed an active response to interferons (IFNs; **Fig. 5a-b, Extended Data Fig. 5a)**. IRF1 is an IFN-responsive transcription factor that translocates from the cytoplasm to the nucleus and MX1 and MHC-I are downstream response genes; MX1 forms multiple biomolecular condensates in each cell[15] and MHC-I is found on the cell surface. The inferred IFN-positive domains were ~50 to 100 µm in diameter, implying highly localised cytokine activity (domain size was confirmed on a distant serial section; **Extended Data Fig. 5b-d**)**.** Within these domains, melanocytic cells had started to pass through the DEJ and were in contact with immune cells (**Fig. 5b-c)**. Thus, our data provide direct evidence for restricted and recurrent spatial niches, defined by the simultaneous presence of an IFN response, melanocyte-immune cell contact, and melanocytes crossing the DEJ (the first step in invasion). These IFN-positive spatial niches were coincident with the lineage switching described above but without detectable spatial correlation, despite evidence that IFN can induce melanoma de-differentiation in cultured melanoma cells[37].

Progenitor and effector T-cell subsets

The normal epidermis has an abundance of resident memory T cells as a consequence of prior encounters with non-tumour antigens (these T_{MEM} cells are characterized by expression of the lineage markers CD45RO and CD103)[38]. The presence of tumour leads to additional T-cell recruitment and activation. In-depth 3D immunoprofiling of metastatic melanoma using ten T cell lineage and state markers (n=4,710 CD8 and 2,820 CD4 cells) revealed a remarkable diversity of populations and states (**Fig. 5d-j, Extended Data 5e,f**). Among these, T_{PEX} cells[39–41] (15% of CD8 cells; orange box; **Fig. 5k**) are of particular interest because they can be re-activated by immune checkpoint inhibitors (ICIs) and their presence is associated with improved patient outcomes[42].

These cells are defined as $CD8^+$ $CD3^+$ T cells co-expressing the master transcriptional regulator T Cell Factor 1 (TCF1)[43] and checkpoint proteins (exhaustion markers) PD-1 and LAG3. In our data, T_{PEX} cells could be divided into two subpopulations based on expression of CD45RO and CD103; two CD proteins that are traditionally markers of tissue-homing memory cells (T_{MEM}; magenta box). Thus, T_{PEX} and T_{MEM} populations overlapped (giving rise to the hybrid populations T_{POP1} and T_{POP2}; **Fig. 5k).** T_{MEM} cells also overlapped effector T cells (T_{EFF}; blue box; defined as $CD8^+$ $TCF1^-$ $PD1^+$ $[LAG3 \text{ or } TIM3]^+$ [Ki67, PCNA, and/or $GZMB]^+$) and gave rise to hybrid populations T_{POP3} and T_{POP4}. Terminally exhausted cells (T_{EX}; grey box; defined as $CD8^+$ $PD1^+$ $[LAG3 \text{ or } TIM3]^+$ [$Ki67^-$, $PCNA^-$, and $GZMB^-$]) were distinct from the four hybrid populations. Thus, T_{PEX}, T_{MEM}, and T_{EFF} CD8 T cell populations, which are commonly described as functionally distinct, appear to have a substantial overlap. Analogous results were obtained for CD4 T cells (**Extended Data Fig. 5g**).

Cytotoxic T cells could be distinguished by the presence of 1-20 GZMB puncta per cell (**Extended Data Fig. 5h**). Unexpectedly, $GZMB^+$ cells (5% of all CD8 T cells) were found in T cells that were both positive or negative for TCF1, CD45RO, and CD103 (**Fig. 5l** red bars). While $TCF1^-$ cells were more likely to be $GZMB^+$ and in contact with tumour cells than any other subtype. visual review confirmed that cells in all four populations exhibited polarization of GZMB toward closely apposed tumour cells, implying active cell killing. T_{PEX}, T_{MEM}, and T_{EFF} cells were also highly proliferative (40-80% PCNA or Ki67 positive) demonstrating a high degree of activation and self-renewal. Moreover, greater than 60% of all CD8 T cells contained multiple MX1 puncta as a result of an active response to IFN (**Fig. 5l;** yellow bars). These data are consistent with the known effects of IFN on T cell proliferation and suggest that this extends to all major T cell subtypes.

Spatial analysis showed that T_{PEX} cells were significantly closer to T_{MEM} and T_{EFF} cells than to T_{EX} or other T_{PEX} cells (**Extended Data Fig. 5i,j**). T_{MEM} cells were the most likely to be close to tumour cells (**Fig. 5k, Extended Data Fig. 5k).** These data are consistent with evolution of T_{PEX} cells from a $TCF1^+$ to a $TCF1^-$ effector status in both the memory-related (T_{POP2} $CD45RO^+$ $CD103^+$) and classical (T_{POP1}) populations (**Extended Data Fig. 5l,m**). Thus, we infer that differentiation of T_{PEX} cells involves three branches, one involved in self-renewal, one in direct generation of $TCF1^+$ cytotoxic cells, and the third giving rise to classic T_{EFF} cells.

Membrane-membrane interactions

Existing approaches to proximity analysis use nuclear positions to identify cell-cell interactions[18] but high resolution imaging made it possible to detect the more biologically relevant process of membrane-membrane interaction. Three arrangements were observed: (i) direct binding (Type I interaction) (ii) membrane apposition (Type II) and (iii) neighbourhood clustering (Type III). Direct binding involved pixel-level overlap in membrane proteins from neighbouring cells. This was most obvious in the case of a $CD8^+$ $PD1^+$ T cells interacting with PDL1 expressing cells; **Figure 6a** shows this for a rare $PDL1^+$ melanocytic cell. A line integral across the cell-cell junction, followed by

polynomial curve fitting, revealed a membrane-to-membrane spacing of ~70 nm (**Fig. 6b**) vs. an average intermembrane spacing of ~1.5 µm among all cells. PDL1 expressing dendritic cells bound to $CD8^+$ $PD1^+$ T cells had a similar membrane spacing (**Fig. 6c,d**), as did a T cell interacting with a PDL1 negative melanocytic cell in the VGP (**Fig. 6e,f, Extended Data Fig. 6a**). Given the resolution of our microscopy, these spacings are consistent with EM of juxtracrine signalling and immunological synapses involving integrin-stabilised cell-cell contacts and intervening clefts with ~30 nm membrane separation[44].

A second form of cell-cell interaction was characterized by neighbouring cells with extensive membrane apposition but without evidence of pixel-level overlap in protein staining; in this case a membrane-membrane spacing of 300-600 nm was typical (**Fig. 6g,h**). Type II interactions between CD4 and CD8 T cells were common across the MIS, without evidence of a nearby antigen presenting cell (e.g., dendritic cell), making this an atypical interaction with respect to current understanding of T cell biology. In the conventional mode, APCs present antigens to both CD4 and CD8 T cells, with the CD4 helper cells enhancing the cytotoxicity of CD8 cells via cytokine production.

A third form of cell-cell interaction involved an intermembrane spacing of ~500 nm but only along a small area of the membrane (1-2 μm^2); such interactions could involve 100 or more immune cells, a pattern we have described previously as lymphocyte networks (lymphonets)[6]. We observed lymphonets comprised primarily of CD4 T cells or CD8 T cells, dendritic cells, and mixtures thereof (**Fig. 6i-l, Extended Data Fig. 6b**). Lymphonets did not contain $CD4^+$ $FOXP3^+$ regulatory T cells, which were most commonly involved in Type I interactions (**Fig. 6k**), or tissue-resident macrophages, which uniformly distributed across the dermis. Type III interactions among T, B, and dendritic cells were also observed in VGP melanoma (**Fig. 6l**) and likely represent nascent tertiary lymphoid structures (TLS), which have recently been shown to play role in the responsiveness of metastatic melanoma to immunotherapy[45].

These three classes of membrane-membrane interaction co-occurred. **Figure 6m-n** shows a complex set of cell-cell interactions involving a melanocytic cell at the DEJ (cell 1) and 10 immune cells (cells 2-11; **Fig. 6o, Supplementary Video 5**). In this network, a $CD4^+$ $GZMB^+$ memory T cell (cell 2) formed a Type I contact with a $CD8^+$ $LAG3^+$ $CD103^+$ $PD1^-$ memory T cell (cell 3; **Fig. 6p**) with an estimated membrane-membrane spacing of 30 nm over a 20-30 um^2 area (**Fig. 6q)**. Cell 3 made an extended Type II contact with another memory $CD8^+$ $CD103^+$ $LAG3^+$ $PD1^-$ T cell (cell 5; 150 nm spacing **Fig. 6r**). Cell 4 and 5 engaged in a spatially restricted Type III interaction (640 nm spacing; **Extended Data Fig. 6c**). CD4 T cell 2 also engaged in Type II contact with a melanocytic cell (1; 690 nm spacing; **Fig. 6s,t**). The two cells were proximate over a much larger area, but we judged the 1.1 µm spacing to be a consequence of tissue packing rather than interaction (**Fig. 6u**). Elsewhere in the network, Type I interactions were observed between CD4 T cell 5 and a dendritic cell (cell 6) and cell 6 and a CD4 T_{REG} cell (cell 8); finally, a $CD8^+$ network (cells 9-11) extended in

an epidermal direction (**Fig. 6o**). The distinctions among types of membrane interaction were not always unambiguous and, given the dynamic nature of cell-cell communication, different interaction classes may represent different points in the time of evolution of a common structure. Regardless, our data show that immune cells can form complex simultaneous associations with cells of different types including those known to send both positive and negative signals to cytotoxic T cells.

Conclusions

Traditional 5 µm tissue sections contain few if any intact cells and this substantially interferes with detailed phenotyping of tightly packed tissues. However, increasing thickness to 30-40 µm enables intact cells to be studied while retaining compatibility with conventional high-resolution confocal microscopy. Under these circumstances, neighbourhood analysis can be based on interaction of juxtaposed membranes rather than nuclear position. Because high resolution imaging is inherently 3D, thick section tissue imaging makes it possible to study intracellular organelles, condensates, cytoskeletal structures, receptor-ligand complexes (including targets of therapeutic drugs), networks of filipodia and dendrites, changes in cell adhesion, and precise protein distributions in diverse cell types and tissues. These are processes that have hitherto been amenable to study primarily in cultured cells.

Precise 3D phenotyping of tumour and immune cells provides new insight into cancer initiation and immunosurveillance. Melanocytic cells in MIS expressed every possible combination of the six lineage and epigenetic markers we assayed, implying a high degree of plasticity in morphology and cell state. Plasticity is well-described in late-stage melanoma and cell lines[46], but our data suggest it is also a feature of early stage disease. One state missing from our primary melanomas but present in metastases is an NGFR-high state, which has been described as neural crest (stem-like) and tumour-initiating. Thus, high cell plasticity may precede the appearance of stem-like states rather than derive from them. T cells are also found in a wide range of states, with overlap between precursor, effector, and memory subtypes. This implies branched rather than linear development, with phenotypic plasticity. Moreover, we find that individual immune cells are often subject to opposing regulatory signals: a single cytotoxic $GZMB^+$ CD8 T cell can be polarized toward a tumour cell, enveloped by filipodia from a CD4 helper cell, and repressed by a PDL1-expresing myeloid cell. Lineage plasticity overlaps (but not obviously correlates) with spatially restricted inflammatory domains, which are often only a few cell diameters wide. Spatially restricted cytokine signalling is predicted by mathematical models of cytokine production and uptake under conditions of high consumption[47].

Thick section 3D imaging can be performed using a variety of confocal microscopes on diverse archival human tumours. An important next step will be linking cell and tissue morphologies visible in high resolution 3D images to specific functions. This will likely involve pairing high-plex imaging of tissues with cell cultures or mouse models subjected to perturbational experiments. Immune cell

states distinguishable by imaging also need to be mapped to single-cell transcriptional states. We envision using thick-section high-plex imaging in combination with large-scale serial section reconstruction[48,49] or light sheet microscopy[50] to provide broader tissue context. However, high plex 3D imaging is likely to remain a complement rather than a replacement for simpler 2D methods. In particular, 3D data can serve as a ground truth for training computational models able to discriminate otherwise ambiguous states in 2D images and correct for limitations in 2D images that might confound accurate biological interpretation.

Acknowledgements

We thank T. Kupper, D. Liu, and J. Agudo for scientific advice, A. Chen, S. Chan, J. Muhlich, and J, Hoffer for help with data analysis, N. Ghelenborg and E. Moerth for pre-publication access to a 3D Vitesse data viewer, J Lian for model training, and J Appelt for tissue integrity studies. We thank the MicRoN core facility at HMS and G. Guimaraes, T. Desai, and S. Fore from Carl Zeiss Inc. for providing access to an LSM980 Airyscan 2 microscope.

Funding

This work was supported by Ludwig Cancer Research and the Ludwig Center at Harvard (P.K.S., S.S.) and by NCI grant U2C-CA233262 (P.K.S., S.S.), R00CA256497 (A.J.N.), Research Specialist Award R50-CA252138 (Z.M.) and CCBIR grant U54-CA268072 (G.D., P.K.S and S.S.). Histopathology was supported by P30-CA06516. Development of computational methods and image processing software is supported by a Team Science Grant from the Gray Foundation (P.K.S., S.S.), the Gates Foundation grant INV-027106 (P.K.S.), the David Liposarcoma Research Initiative at DFCI supported by KBF Canada via the Rossy Foundation Fund (P.K.S., S.S.), and the Emerson Collective (P.K.S.). S.S. is supported by the BWH President's Scholars Award.

Author Contributions

CY, PKS, and AJN developed the concept for the study. CY, ZM and PML collected image data. FZ and GD developed software and performed data analysis in collaboration with CY and AJN. SS GFM and CGL provided specimens and pathology expertise. All authors wrote and edited the manuscript. GD, GFM, CGL, SS and PKS provided supervision.

Competing Interests

PKS is a co-founder and member of the BOD of Glencoe Software, member of the BOD for Applied Biomath, and member of the SAB for RareCyte, NanoString, Reverb Therapeutics and Montai Health; he holds equity in Glencoe, Applied Biomath, and RareCyte. PKS consults for Merck and the Sorger lab has received research funding from Novartis and Merck in the past five years. The other authors declare no outside interests.

Materials & Correspondence

All materials associated with this study are available through commercial vendors. Please contact Peter Sorger (peter_sorger@hms.harvard.edu) with any additional requests.

Data Availability (At time of publication)

All images and derived data (~3 TB) are available without restriction via the NCI Human Tumor Atlas Network Portal (data.humantumoratlas.org/). The Human Tumor Atlas Network participant (specimen) ID numbers are listed in **Supplementary Table 2**. All other data supporting the findings of this study are available via an index page on GitHub that has been archived on Zenodo (doi.org/10.5281/zenodo.10055593). To see a 2D maximum projection of a subset of this data in the MINERVA in-browser viewer (no download required), please go to www.tissue-atlas.org/mel-3d-mis-2 (see screenshot, below). See https://www.minerva.im/ for more information on how to use the MINERVA viewer. We are also implementing 3D interactive viewing of data from specific figure panels within the browser-based tool Vitessce[51,52] (http://vitessce.io/). Links to figures panels 3a, 3d, and 6n can be accessed at the links below (*see second screenshot, below for example of figure 3a).* This is a work in progress that should be ready by time of publication and combines primary data with surface meshes.

Figure 3a - http://beta-3d.vitessce.io/?dataset=Figure3a_blood_vessel

Figure 3d - http://beta-3d.vitessce.io/?dataset=Figure3d_tumor_cytoskeleton

Figure 6n - http://beta-3d.vitessce.io/?dataset=Figure6n_cell_community

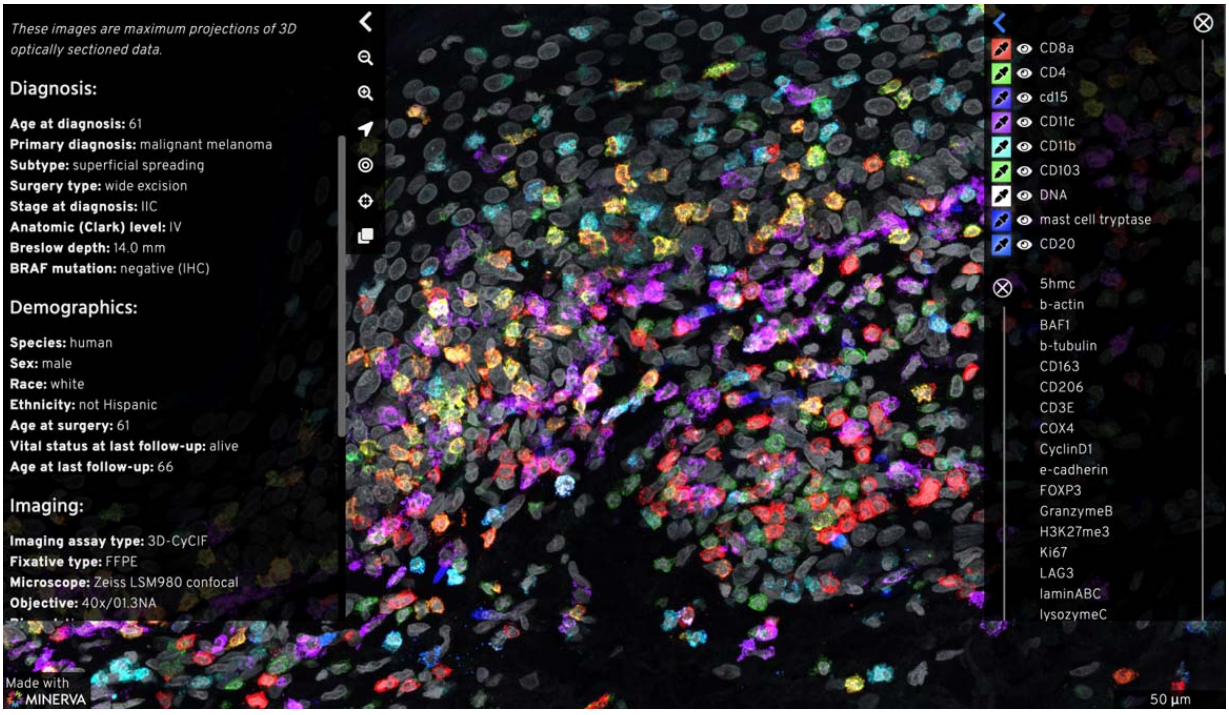

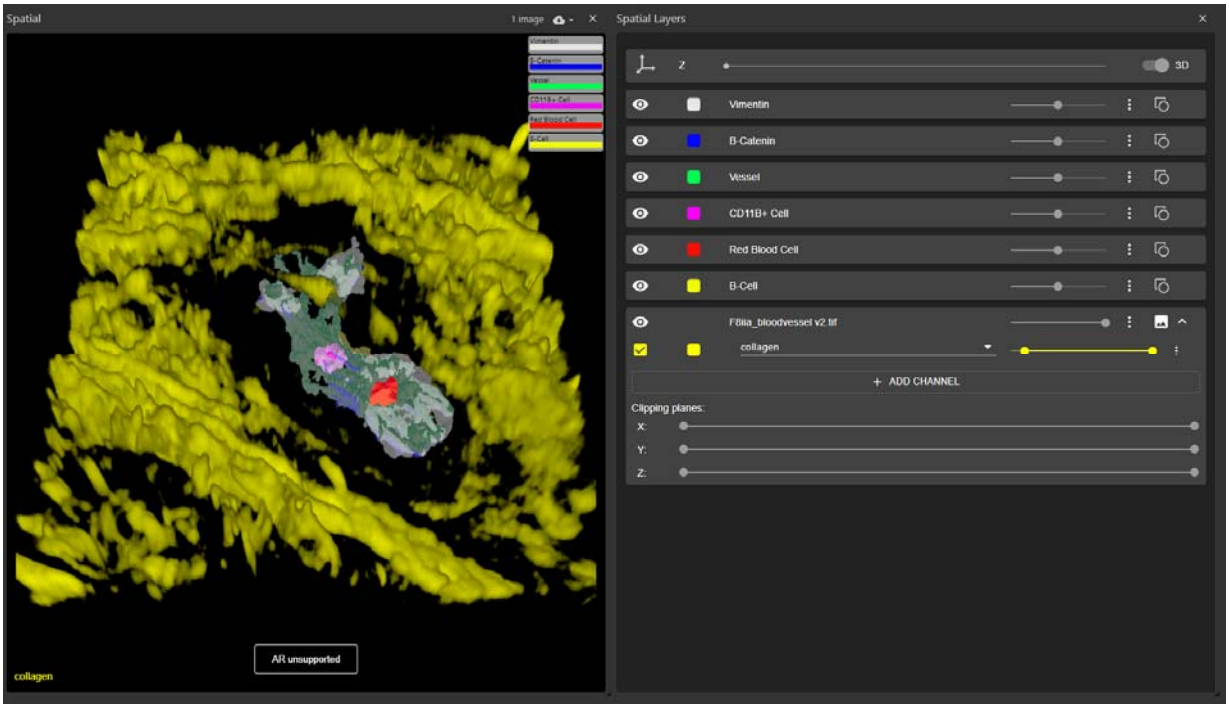

Code Availability

Original code associated with this paper is available on GitHub (github.com/labsyspharm/mel-3d-mis) and Zenodo (doi.org/10.5281/zenodo.10055593).

Figure Legends

Figure 1: Demonstrating the need for thick tissue sections using 3D CyCIF. **a,** Surface rendering illustrates the nuclei volume of 5 µm (left) and 35 µm tissue sections (right). Scale bars, 10 µm. **b,** Immunofluorescence images of 6-marker subsets illustrating the microenvironment of the cellular community from the VGP highlighted in **c-d** (dotted lines). **c,** 3D rendering of 3 selected cells from (**b**). Comparison of the point spread function and optical planes (cyan) for laser scanning confocal and widefield microscopy shown. Upper: x,z (side) view. Lower: y-x (top) view. **d,** Synthetic 5 µm sections of 3-dimensional data in x-z (center) and x-y 2D projections (red outlines to left and right; labelled I-V). Simulated widefield slice III image using theoretical PSFs (lower left, white outline). **e,** Multi-modal image integrating 3D CyCIF with second harmonic signal of collagen highlighting the melanoma in-situ region (MIS). Maximum intensity projection of selected channels at lower magnification (left), with additional marker subsets for the indicated ROI (right). Scale bar, 100 µm. **f-h,** FOVs capturing the boundary of a vertical growth phase tumour, highlighting the densely-packed tissue at low-resolution (**f**) and high-resolution renderings of an individual cell (**g-h**). **i-k,** Examples of cells with multiple processes in melanoma: **i**, Cluster of CD8 T cells in metastatic melanoma. **j,** Dendritic cell with filopodia extensions in metastatic melanoma. Two filopodia making contact with a T cell and tumour cell, labelled with arrows or arrowheads, respectively. **k,** Langerhans cell in the MIS. Scale bars 5 µm.

Figure 2: Visualizing complex organelle and cell-surface morphologies. a-f, Selected channels of 54 plex 3D CyCIF images used for identifying cell types and organelles. All cells found in the dermis of the MIS (full marker assignment in **Supplementary Figure 12**)**. a-c,** Maximum projections of a neutrophil showing marker subsets for identifying organelles (**a**), a multi-lobed nucleus (**b**), the cytoskeleton (**c**). **d,** A 3D rendering of the cell shown in (**a-c**). **e-g,** 3D rendering and maximum intensity projection inset (upper right) for selected cells, including neutrophils in the MIS (**e** & **f**) and a T cell in metastatic melanoma (**g**). **h,** 3D rendering of a neutrophil interacting with a MART1^{+} tumour cell (magenta) in the MIS. **i-l,** Distribution of intracellular (**i** & **k**) and membranous (**j** & **l**) markers in a single cell as maximum projections (**i-j**) and surface rendering (**k-l**). **m,** Surface rendering of five interacting immune cells in the MIS, including three CD4^{+} helper T cells (magenta-translucent) and two CD8^{+} T cells (cyan-opaque). Also shown, MX1 biomolecular condensates (green), globular GZMB^{+} (yellow) in CD4^{+} T cells. Spacing between opposed membranes is <1.5 µm and contact area is ~20µm^{2}. Scale bars 5 µm. See **Extended Data Figure 2c** for reversed T cell opacity. **n-o,** Two CD4^{+} T cells from the VGP interacting expressing PD1 and PDL1 as a maximum projection (**n**) and transparent surface mesh showing contact area, with colocalized PD1 and PDL1 shown as spheres. **p,** CD8^{+} T cell (red) and dendritic cell (purple) interacting with a tumour cell with long filopodia. **q,** Same cells as (**p**) with GZMB, PD1, and LAG3 shown, highlighting that the T cell is activated and cytotoxic. **r,** surface rendering of interactions in (**p**) and (**q**), showing the filopodia in greater detail. **s,** Multicellular interaction in metastatic melanoma. A dendritic cell interacting with a

tumour cell (with surface rendering overlaid onto immunofluorescence) and a CD4 T_{helper} cell interacting with a CD8 T cell through filopodia (shown in greater detail in inset). **t,** Same field of view in (**s**), showing PD1 and PDL1 colocalization between CD8 T cell and dendritic cell (blue arrow). In the CD8 cell, GZMB is polarized towards the tumour cell (green arrow and inset). Location of inset shown by box with dotted line. Scale bars as indicated.

Figure 3: Visualizing the interplay of multi-cellular structures, cell shape, motility, and tension in native tissue. a, Surface rendering of a segment of an intact blood vessel within the MIS region. Dashed lines demarcate cutting planes for cross-sectional views (insets), illustrating the capability to distinguish between internal components of the blood vessel: a helper T (2), dendritic (1) cell, neutrophil (4), red blood cell (6) and external, fully intact B cell (5). Scale bar, 10 µm. **b,** Representative $CD20^+$ B cell (magenta) with elongated morphology interacting closely with collagen fibres (yellow), as a maximum intensity projection. Scale bars, 5 µm. **c,** Tukey box plot illustrating the distances between collagen fibres and different cell types in the MIS. Statistical significance was assessed using one sided unpaired student's *t-test*. Centre line, median; box limits, upper and lower quartiles; whiskers, minimum and maximum after removing outliers. **d,** An orthogonal slice of a VGP melanoma region, highlighting the punctate nature of β-actin in tumour cells and the generally elevated expression levels of β-actin in immune cells, alongside graded pMLC2 expression. Scale bar 20 µm. **e,** High resolution insets of FOV indicated in (**d**) and (**f**), highlighting elevated β-actin expression in dendritic cells (1) and CD8 T cells (2), β-actin puncta in $SOX10^+$ tumour cells (3), and alternating patterns of pMLC2 and E-cadherin (4-6). Scale bars 5 µm. **f,** Orthogonal slice of the same region as (**d**), highlighting the inverse expression of pMLC2 and ECAD, and the locations of T cells and tumour cells. Scale bar 20 µm.

Figure 4: Melanocyte morphologies, lineage marker expression, and cellular interactions in the melanocytic intraepidermal compartment. a, Surface-rendered melanocytes within the MIS, illustrating variations in conventional dendritic-like and rounded morphologies. Scale bars, 5 µm. **b,** A representative FOV showcasing the transition of melanocyte morphology from dendritic-like at the DEJ to compact (bottom), and ultimately rounded, during the pagetoid spread within the epidermis (top). Scale bars, 10 µm. **c-h**, Representative examples of PRAME- and MART1-expressing pagetoid spread cells showing different expression levels of 5hMC, SOX9 and SOX10. Markers as indicated on each panel. Scale bars, 5 µm, **i-p**, Images of the MIS. Left column: segmentation masks coloured by marker intensity and brightness representing mean expression level. Masks in grey denote the positions of keratinocytes; dashed circles denote IFN-rich domains. Markers as indicated on each panel. Right column: high-resolution immunofluorescence images of the same markers per row. **q,r,** Images as in **l-p** but with magenta denoting cells containing nuclear actin rods. **s,** Bar graph showing the number of melanocytic cells in the MIS positive for each of 63 combinations of marker proteins. MART1 (green), PRAME (yellow), MITF (orange), SOX10 (red), SOX9 (blue), and 5hmc (violet). Note different y-axes. **t**, Maximum projection of a region from the

vertical growth phase showing variability of SOX9 (red) and SOX10 (green) expression. Scale bar, 30 μm.

Figure 5: Spatial analysis of IFN-rich domains and distinct T cell lineages. a, Three selected channels of 54-plex CyCIF image of the MIS in dataset 2 (LSP13625). A single image plane from the middle of the specimen is shown. IFN-rich domains denoted by dashed circles. DEJ denoted by white dashed line. Scale bar 100 μm. **b,** Magnified view of inset from panel **a** showing coincident nuclear localization of IRF1, expression of MX1, and MHC-1 upregulation. DEJ denoted by white dashed line. White arrowheads indicate invading melanocytic cells into dermis. Scale bars, 50 μm. **c,** Enlarged inset from panel (**a**) showing diversity of immune cells crossing the DEJ. DEJ denoted by white dashed lines. **d,e,** Max projection of an activated T_{PEX} cell, showing intracellular organelles like GZMB (**d**) and membranous proteins such as LAG3 and PD1 (**e**). **f,** 3D rendering of a T_{MEM} cell interacting with a T_{PEX} cell, which is in turn interacting with a cluster of metastatic melanoma tumour cells. Dendritic cells surround the neighbourhood. **g-j,** The T_{MEM} and T_{PEX} cells shown in (**f**), as a maximum projection (**g** & **h**) and 3D rendering (**I** & **j**). **k,** Hierarchical tree diagram showing proportions of CD8 T sub-lineages the metastatic melanoma specimen. T_{MEM} (magenta), T_{PEX} (orange), and T_{EFF} (blue) subtypes overlap, giving rise to four hybrid populations (T_{POP1-4}) as denoted by vertical labels. See text for details. Red arrows denote additional cell subsets that are not shown on this tree. **l,** Percent of cells positive for GZMB (red) or MX1 (yellow) by population.

Figure 6: Cell-cell interactions and multivalent immune cell niches. a-h, Selected fields of view and surface renderings from dataset 1 (LSP1362). **a,** A single image plane of a $PD1^+$ dendritic cell (cell 1) interacting with two $MART1^+$ tumour cells. White arrow denotes juxtacrine PD1-PDL1 interaction. Scale bar 5 μm. **b**, Line integral of interaction of cells 1 and 3 in **a**. **c-d,** A dendritic cell (cell 1) interacting with a $CD8^+$ T cell as a maximum projection I and line integral (**d**). Box indicates region of line integral shown in **d**. **e,f,** Representations of a T_{PEX} cell from the invasive margin as a maximum projection (**e**) and line integral across membrane (**f**), for region marked by white dashed box in I. **g,h,** A conventional direct interaction between a CD4 helper T cell (magenta) and a dendritic cell (yellow), as a maximum intensity projection (**g**). The degree of direct interaction is shown by line integral in (**h**). **i-k,** Examples of Type III interactions (lymphonets), involving $CD4^+$ $CD8^+$ dendritic cells in the MIS. These networks are characterised by cell-cell interactions involving immediate contact through relatively small membrane domains and a loosely packed arrangement. **l,** Stroma in the vicinity of the VGP melanoma showing neighbourhoods rich in $CD20^+$ B cells, $CD11C^+$ dendritic cells, $CD3E^+$ T cells but without the clusters of proliferating $Ki67^+$ cells that are characteristic of mature germinal centres. **m-o,** 11 cells from the MIS lying in proximity to the DEJ, shown as primary data (**m**), 3D surface renderings (**n**), and as a schematic representation of three Type I, four Type II, and two Type III interactions inferred from line integrals in single-plane images (**o**). Scale bars, 10 μm. **p,** A cross-sectional slice of the two $CD8^+$ T cells and two $CD4^+$ featured in (**m**), depicting the direct engagement of cell membranes. Scale bar 3 μm. **q,r,** A line integral plot

depicting CD4 and CD8 average expression within the bottom boxed region of **p** (**q**) or right boxed region of **r** (**s**). **s-u,** A Type II interaction between a MART1^{+} tumour cell and CD4^{+} T cells, as a representative image (**s**) and line integrals for the interaction between cells 1-2 at region A (**t**) and B (**u**). Scale bars, 3 μm. Red 'X's mark the maximum intensity along line integral and denotes the boundary of the cell membrane for each channel.

Extended Data Figure Legends

Extended Data Figure 1: Demonstrating the need for thick tissue sections using 3D CyCIF. **a,** Individual channels of simulated Ψ 2D widefield (10x/0.45), see **Figure 1d** for composite image. **b,** UMAP rendering of all cell types analysed in Dataset 1 (LSP13626). See **Supplementary Figure 12** for flow chart of cell type classifications. **c,** 2D CyCIF whole slide image of adjacent section of the primary melanoma sample HTA7_1. White squares indicate the regions of melanoma in-situ (MIS) and the invasive vertical growth phase (VGP) melanoma where high-resolution 3D CyCIF was performed. Marker colours as indicated. Scale bar 1 mm. **d,** Maximum projection of the region of the invasive margin imaged with 3D CyCIF of Dataset 1 (LSP13626), showing a subset (6) of the total 54 markers. Image corresponds to right ROI indicated in (**c**). Scale bar 100 μm. **e,f,** Dendritic cell from **Figure 1j** with additional markers highlighting T cell subtypes (**e**) and the dense neighbourhood of tumour cells (**f**). **g,** Mask plots overlaid on the vertical growth phase melanoma region, highlighting spherical cells in yellow and elongated cells in magenta and cyan. Scale bar, 100 μm. **h,i**, Surface renderings of selected cells from **g**.

Extended Data Figure 2: Visualizing complex organelle and cell-surface morphologies. a, 3D rendering of a neutrophil with organelles shown. **b,** Histogram displaying the frequency distribution of LAG3 spots per cell. The x-axis represents the number of LAG3 spots identified within individual cells, and the y-axis indicates the frequency of cells corresponding to each LAG3 spot count. **c,** Surface rendering of five immune cells involving Type II interactions among three CD4^{+} helper T cells (magenta-opaque) and two CD8^{+} T cells (cyan-translucent), identical to **Figure 2m** but with transparency reversed. Also shown, punctate LAG3 (yellow) on the membranes of CD8^{+} T cells. **d-f,** Volumetric renderings showing PD1 and PDL1 can manifest as different morphologies within the same sample (Dataset 3 - LSP22409). **d**, diffused PDL1. **e**, diffused PD1 and punctate PDL1 within the same immune cell. **f**, colocalization of punctate PD1 and PDL1 within the same dendritic cells. **g,** Activated CD8^{+} T cell with long filopodia (red) and dendritic cell (purple) interacting with a tumour cell. Note: This is a different cell community from those shown in Figure 2p-r. **h,** Same cells as (**g**) with GZMB and LAG3 shown, highlighting that the T cell is not only activated but cytotoxic too. **i,** surface rendering of interactions in (**g**) and (**h**), showing the filopodia in greater detail. **j,** 3D rendering of cells highlighted in the multicellular interactions in **Figure 2s-t**.

Extended Data Figure 3: Visualizing multi-cellular structures, cell shape, and motility in native tissue. a, Surface rendering of 5-micron virtual sections of a blood vessel segment at an angled view (top) and a top view (bottom). *See **Figure 3a** for full vessel from 35-micron thick tissue*. Scale bar 10 μm. **b,** Surface rendering of B cell undergoing diapedesis. B cell (yellow) with elongated nuclei (purple), passing through a blood vessel (green). Scale bar 5 μm. **c,** T cell inside vessel, shown as a rendering (top) and as a 2D maximum intensity projection (bottom). **d**, B cells in the VGP dermis with a characteristic rounded morphology.

Extended Data Figure 4: Actin morphologies in tumour and immune cells in the MIS. a, Three immune cells as a surface rendering with cortical actin shown in red and immune marker in grey (top) and as a maximum projection (bottom). Scale bar, 5 μm. **b-d,** Examples of nuclear actin in melanocytic cells. **b,** Maximum projection of MART1+ melanocytic cells (blue) with nuclear actin rods (red-to-yellow heatmap). Nuclei shown in green. Scale bar 5 μm. **c,** Surface rendering melanocytic cell nuclei (blue) containing actin rods, with individual actin rods indicated with assorted colours. Scalebar 5 μm. **d,** Colour overlay of melanocytic cells containing nuclear actin rods (red) on maximum projection of MART1 (grey). Scale bar 100 μm.

Extended Data Figure 5: Spatial analysis of IFN-rich domains and distinct T cell lineages. a, 2D CyCIF image of the MIS showing the correlation between pockets of MX1 (yellow) and IRF1 (cyan) along the dermal epidermal junction (dark blue). Dendritic cells shown in purple. Scale bar 50 μm. **b,** Quantification of MHC-1 expression in Gray Level Units (GLU) <1.5 μm (proximal) or >1.5 μm (distant) from an MX1 punctum in the DEJ of an independent dataset (dataset 1; LSP13626). Error bar indicates STD. **c,** Five selected channels from 42-plex CyCIF image of MIS in dataset 2. DEJ denoted by white dashed lines. White dashed rectangle is enlarged in **Figure 5c** and exemplifies CD45+ immune cells (green) breaking through the DEJ into the epidermis. Scale bar 30 μm. **d,** Maximum projection of MIS region showing combinations and variability of SOX10 (magenta) and SOX9 (green) expression in melanocytic cells (MART1 – blue). Scale bar 30 μm. **e,f,** Two examples of maximum projections of $TCF1^+$ T_{PEX} cells, showing non-proliferation (**e**) and proliferation via PCNA staining (**f**). Scale bar 5 μm. **g,** Hierarchical tree diagram showing proportions of CD4+ T cell sub-lineages in the metastatic melanoma sample. Red values indicate the percentage of cells in the associated state that are next to tumour cells. **h,** Comparison of GZMB morphology within a CD8 T cell (yellow arrow) and CD4 T cell (white arrow) in the MIS. **i-m** Boxen plots of cell proximity in metastatic melanoma. Each box in a boxen plot represents a quantile range, progressively detailing the distribution from the median outwards to the extremes. Red boxes indicate cells positive for the given marker, blue indicate cells negative for the given marker, white indicate markers that were not used for selection. **i,j,** The distribution of the shortest distance between $CD103^+$ (**i**) and $CD103^-$ (**j**) T_{PEX} cells with other T cell subpopulations. **k,** The distribution of the shortest distance between tumour cells and T cell subpopulations. **l,m,** The distribution of the

shortest distance between $CD103^+$ (**l**) and $CD103^-$ (**m**) T_{PEX} cells with subclasses of T_{MEM} populations, with activity states indicated by the marker patterns on the left.

Extended Data Figure 6: Cell-cell interactions and multivalent immune cell niches. a, Surface rendering of **Fig. 6e. b,** Maximum projection of tertiary lymphoid structures in the VGP tumour region. Dashed lines demarcate colonies of CD20+ B cells (cyan) mixed with CD11C+ dendritic cells (yellow). White box indicates zoom in version found in **Figure 6l**. Scale bar 100 μm. **c,** A line integral plot depicting CD4 (cyan) and CD8 (magenta) average expression across membranes of cells 4 (CD8 T cell) and 5 (CD4 T cell) from **Figure 6p**. Solid lines from raw data, dashed lines are from polynomial curve fitting. Red 'X's mark the maximum intensity along line integral and denotes the boundary of the cell membrane for each channel.

Extended Data Figure 7. Recurrent cellular neighbourhoods, identified by applying spatial latent Dirichlet allocation (LDA) to 2D projections of 3D data. a, Scatter plot showing the MIS region. Cells are coloured based on their recurrent cellular neighbourhoods (RCN1–7). **b,** Scatter plot highlighting the distribution of each RCN in the MIS region of tissue. **c,** Scatter plot showing the invasive region of vertical growth phase melanoma. Cells are coloured based on the RCN to which they belong. **d,** Scatter plot highlighting the distribution of each RCN in the invasive region of tissue. **e,** Bar plot depicting the proportion of different cell-types within each RCN.

Supplementary Videos

Supplementary Video 1: Surface rendering of Hoechst stained 5 and 35-micron thick serial sections from primary melanoma. 3D rendering from Bitplane Imaris 10.0.

Supplementary Video 2: Surface rendering of an intact blood vessel (green) from the MIS region with B cell (yellow), red blood cell (red), and neutrophil (pink). 3D rendering from Bitplane Imaris 10.0.

Supplementary Video 3: Volumetric rendering of packed tumour cells from the invasive margin. Rendering from Bitplane Imaris 10.0. Marker colours as indicated.

Supplementary Video 4: Surface rendering of CD4 (magenta) and CD8 (blue) positive T cells with LAG3 (yellow spheres), MX1 (green sphere), and GZMB (yellow blobs). Rendering from Bitplane Imaris 10.0.

Supplementary Video 5: Surface rendering of 1 melanocytic cell (green) and 10 interacting immune cells comprising of CD4 T cells (blue), CD8 T cells (magenta), and dendritic cells (yellow) from the MIS region. Rendering from Bitplane Imaris 10.0.

Supplemental Tables

Supplementary Table 1: Definitions of all protein abbreviations.

Supplementary Table 2: Sample metadata and HTAN identifiers.

Supplementary Table 3: CyCIF antibody panel used for LSP13626 MIS and VGP datasets, the first serial section from a patient with cutaneous melanoma.

Supplementary Table 4: CyCIF antibody panel used for LSP13625 MIS and VGP datasets, the first serial section from a patient with cutaneous melanoma.

Supplementary Table 5: CyCIF antibody panel used for metastatic melanoma (LSP22409 / WD-100476).

Supplementary Table 6: An index of which figure panels relate to which datasets.

Supplementary Discussion

Other Approaches to Imaging 3D Tissue Specimens

3D imaging challenges the ability to balance between acquisition time, sensitivity, and most notably, reduction of out-of-focus signal that would otherwise reduce contrast. The latter is required for resolving structures in thick tissue along the axial direction, where the axial resolution depends on wavelength, numerical aperture of the objective lens, axial sampling step size, and pinhole diameter in the case of a confocal. Traditional widefield microscopy can be supplemented with deconvolution to reassign out-of-focus signal back to the focal plane, which requires knowledge of the point spread function and is generally suitable for thin samples[53]. Total internal reflection fluorescence (TIRF) microscopy[54,55] can produce high contrast very thin 3D images when used in conjunction with other techniques such as DNA paint, but is limited to only 100 nm beyond the coverslip and is not suitable for highly multiplexed imaging protocols where the tissue is not mounted to the coverslip. More commonly found in research settings are spinning disk[56] and laser scanning confocal[57,58] microscopes where the latter is much slower due to the need to laser raster but provides finer control over the pinhole diameter, and thus, the size of the optical sectioning and the gain in contrast by rejection of out of focus light.

Confocal microscopes are relatively light inefficient; between a widefield and laser scanning confocal, orders of magnitude far fewer photons from the sample are rejected and never reach the detector[59] although newer micro lenses and sensitive detectors are able to recapture much of this signal. Additionally, sample thickness at any given point is fully illuminated regardless of which focal plane is currently being imaged and this significantly contributes to photobleaching and challenges in downstream quantitative measurements. In specialized research settings, two-photon excitation (TPE) microscopy[60] uses pulsed mode-locked lasers to excite a femto-litre sized volume via the simultaneous absorption of two photons (typically in the near-infrared range). Two-photon lasers can also capitalize on certain collagen types that emit a label-free second harmonic signal[61–63]; the resulting signal has a wavelength that is precisely half of the incident laser wavelength. Since near-infrared wavelengths experience less attenuation and contribute to less phototoxicity, TPE is preferred in tissue and intravital imaging. Furthermore, multiple fluorophores can share similar two-photon excitation spectra, therefore, this creates a throughput advantage in thick specimens. However, these systems are less common than confocal microscopes because they are significantly costlier and require specialist knowledge to operate and maintain.

A computationally-intensive solution to combine high-plex imaging with coarse 3D data has been to register several thin serial sections,[49,64–66] however, the axial resolution of the final dataset is on the order of 5-20 microns and, thus, consists of incomplete cell volumes. A variety of Light Sheet Fluorescence Microscopy (LSFM) and tissue clearing methods[67–69] have been developed to image tissue sections as thick as several mm, with the most recent capable of subcellular resolution, but

not all clearing methods are compatible with FFPE tissue[70] and the total number of fluorophores that has been imaged is up to 5 or fewer depending on the optics[71,72]. While spectral unmixing, spillover compensation, or the use of Raman dyes can increase this number to 8-10 channels[73–75], to date, sequential staining and high-plex high-resolution (sub-micrometer scale) imaging of thick sections has not been demonstrated.

Given all of these considerations, it was not self-evident that confocal microscopy would be suitable for high-plex imaging of thick tissue sections. We are of efforts to create specialized multiplexed deep imaging microscopes, but the our data suggest that an existing Zeiss LSM980 Confocal microscope can be used for CyCIF with few compromises in terms of sensitivity, speed or resolution. We note that the current work does not fully exploit the spectral ummixing capabilities of the LSM980 and that this awaits further development of antibody panels.

Methods

Specimen collection

Specimens for melanoma (MIS and VGP), glioblastoma, lung metastasis, and tonsil were retrieved from the archives of the Department of Pathology at Brigham and Women's Hospital and collected under Institutional Review Board approval (FWA00007071, Protocol IRB18-1363) under a waiver of consent. Three datasets were used for all experiments: two 35 µm serial sections of melanoma (referred to as Dataset 1 (LSP13626) and Dataset 2 (LSP13625)) and a 35 µm section of metastatic melanoma from the NIH Cooperative Human Tissue Network (CHTN) (referred to as metastatic melanoma or dataset 3; LSP22409 / WD-100476). Serous Tubal Intraepithelial Carcinoma (STIC) samples were obtained from University of Pennsylvania. Quantifications are based on Dataset 1. Deep immune cell phenotyping is based on Dataset 3. See **Supplementary Table 2** for clinical metadata regarding this specimen and the related HTAN identifiers. The histopathological regions of interest for each specimen were annotated from a serial section consistent with the work of Nirmal, Vallius, Maliga et al. (2022)[18] by a board-certified pathologist based on melanoma diagnostic criteria. See **Supplementary Table 6** for an index of which figure panels relate to which datasets.

Cyclic immunofluorescence (CyCIF)

The procedure for thick section CyCIF is similar that of standard CyCIF[76] except that additional care is taken during staining steps (see below) A staining plan containing a list of antibodies used can be found in **Supplementary Table 3-5**. Antigen retrieval, staining, and bleaching was performed as described previously.[18]. Due to the fragile nature of thicker samples, extra care was taken during washes, bleaching and decoverslipping. We found that most tissues held up well, but that a subset of skin and melanoma samples disintegrated during antigen retrieval. We have observed this previously with skin and primary melanoma, and 3D imaging showed that these specimens had not fully adhered to the cover slip, instead exhibiting a series of corrugations just above the cover slip with liquid in between. This issue lies in the realm of “pre-analytical variables,” which are common in

histology, and will required additional work to resolve. ,Antibodies for each cycle were diluted in 400 µl of blocking buffer and stained for 8-10 hours to allow for same-day imaging and at room temperature to encourage penetration of antibodies (see below). See **Supplementary Figures 1-11** for the whole slide images of the full dataset for each sample.

Optimization of sample thickness and antibody staining protocol

We sought to determine an ideal tissue thickness for CyCIF imaging using well-characterized tonsil sections. Based on the maximum working distance of most water and oil-immersion lenses (~200 µm) and the thickness of a grade 1.5 coverslip (170 µm), we obtained tonsil sections that were 10 µm, 20 µm, 30 µm, 35 µm, and 40 µm thick (**Supplementary Fig. 13**). These were stained with Hoechst and y-tubulin conjugated in Alexafluor 555. Gamma-tubulin is punctate and can serve as a useful stain for assessing antibody penetration and image aberration. Z-stacks were acquired for each at 103 nm lateral resolution and 230 nm axial resolution with a 40x/1.2W C-Apochromat water immersion objective lens on a Zeiss LSM980 confocal microscope. We observed punctate gamma-tubulin in all thicknesses up to 35 µm tissue thickness, with uniform intensity along the axial axis (**Supplementary Fig. 13a-d**). However, in the 40 µm thickness, gamma-tubulin appeared to significantly diminish in intensity along the axial axis (**Supplementary Figure 13e**). Furthermore, contrast even at the top surface was poorer than thinner samples. This could suggest that standard dewaxing and antigen retrieval protocols are not suitable for thicknesses greater than 35 µm. With Hoechst staining, we also observed severe signal attenuation in the 40 µm. Unlike gamma-tubulin, excitation and emission light penetration may be the issue here, which is well established for short wavelengths.

We then evaluated if certain fluorophores impacted antibody penetration. This is important for CyCIF where the ability to choose different antibody fluorophore combinations is essential. We obtained a primary melanoma and co-stained MART1 conjugated to Alexafluor 647 with other secondary antibodies (Alexafluor 488, Alexafluor 555, Alexafluor 750) (**Supplementary Fig. 14a**) for 8-10 hours at room temperature. We bleached MART1-647 and restained with Alexafluor 647 in a subsequent cycle. **Supplementary Fig. 14b** shows that the MART1 primary conjugate (magenta) penetrated the full thickness of the tissue, as judged by Hoechst staining (turquoise). **Supplementary Fig. 14c-f** shows that all secondary antibodies (magenta) penetrated equally well and showed a similar staining pattern to the MART1 primary conjugate. This demonstrates the ability for secondary antibodies to be used for thick tissue CyCIF. We noted that Alexafluor 750 had lower contrast, which can be attributed to the lower sensitivity of detectors in the near infrared spectrum.

While testing multiple primary conjugated antibodies, we observed antibody penetration issues with some antibody conjugates. Although many immune markers (PD1, CD11c, CD8a, MHC-1, MHC-II; green) exhibited full depth staining, several tumour and stromal markers (αSMA, PCNA, SOX10; red) only stained the top layer of tissue (**Supplementary Fig. 15**). To determine whether the

fluorophore played a role in this, we repeated staining with the same PCNA clone conjugated to Alexafluor 488 or Alexafluor 750. We noticed there that was a difference in staining pattern; the Alexafluor 488 conjugate stained fewer cells (**Supplementary Fig. 16a**) but showed improved staining penetration (**Supplementary Fig. 16b**). For αSMA, we tried a similar strategy, but using a different fluorophore required a different antibody clone. Unlike PCNA, we did not see an improvement in staining penetration of a blood vessel (**Supplementary Fig. 17**). From these data we concluded that antibody penetration is not uniquely dependent on fluorophore or clone but is influenced by multiple factors and that each antibody must therefore be evaluated for its ability to stain a thick section using Z-stacks.

3D image acquisition

Tonsil and melanoma image data were collected on a LSM980 Airyscan 2 (Carl Zeiss) equipped with a 405nm, 488nm, 561nm, 647nm, and 750nm laser lines, and 10x/0.45NA air and 40x/1.3NA oil immersion objective lenses. In ZEN 3.7, a 2D overview scan using the 10x objective lens was used to identify regions of interest for higher resolution imaging at 40x in 3D. Images were sampled at 16-bit at 0.14 microns per pixel in X and Y, and 0.28 microns per pixel in Z for approximately 170 or more optical planes. The pinhole size was set to 35 microns. At both resolutions, a focus surface was used to maintain focus. To increase throughput, bidirectional and fast frame scanning was used. Channels were separated into two tracks: track 1 - Hoechst, Alexafluor 555, and Alexafluor 750 (if present). track 2 - Alexafluor 488 and Alexafluor 647. The emission range for Hoechst, Alexafluor 488, Alexafluor 555, Alexafluor 647, and Alexafluor 750 were 380nm-489nm, 499nm-544nm, 579nm-640nm, 660nm-705nm, and 755nm-900nm respectively.

Type I and II collagen were imaged using Second Harmonic Generation (SHG) in a Stellaris 8 DIVE coupled to an Insight X3 multiphoton laser and running LasX. Images were acquired with a 20x/0.75NA multi-immersion lens and sampled at 0.36 microns laterally and 0.95 microns axially. SHG signal was detected using 4Tune Spectra non-descanned HyD detectors and separated from that of Hoechst 33342 using Fluorescence Lifetime Imaging Microscopy (FLIM).

Microscope slides were secured in a slide holder fitted with a spring-loaded clamp, which correspondingly was secured onto the microscope stage in a plateholder.

3D image processing and registration

All channels acquired on the Zeiss LSM980 were processed using Zeiss ZEN LSM Plus Processing to improve signal-to-noise. Channels were background subtracted by removing a fixed constant grey-level from the background. The first cycle was stitched in ZEN using the Hoechst channel as a reference, and all subsequent cycles were registered to this first stitched cycle. Single-field and stitched 3D datasets were imported using Bioformats in MATLAB (Mathworks). First, the X and Y translations were obtained using max projections of the Hoechst nuclei channel. Following this transformation, subsequent cycles were registered in Z. We found that separating the lateral from axial transformations was more accurate than registering X, Y, and Z in one optimization step. We

then performed histogram equalization with MATLAB's *histeq()* function and fine-tuned image alignment with elastic deformations using MATLAB's *imregdemons()* function. Lastly, all transformations for each cycle were applied to their corresponding channels. Each channel was saved and appended to a TIFF file and visualized in Meshlab, ChimeraX or Imaris 10.0 (Bitplane) as .ims files.

Single-Cell Phenotyping

Manual gating was performed for each marker to differentiate background from true signal. The gates identified for each marker were subsequently used to normalize the single-cell data within a range of 0 to 1, wherein values above 0.5 indicated cells expressing the marker. The scaled data was subsequently used for phenotyping the cells based on known lineage markers as described previously using the SCIMAP Python package (scimap.xyz).[18] See **Supplementary Figure 12** for the detailed marker combinations used to define cell types.

RCN Analysis to Identify Microenvironmental Communities

The Latent Dirichlet allocation (LDA) based recurrent cellular neighbourhood (RCN) was performed using SCIMAP (scimap.xyz)[18] using a k value of 10 (**Extended Data Figure 7)**. The clusters were manually organized into meta-clusters (7 clusters), based on the cellular composition of the clusters. The meta-clusters were also overlaid on the H&E and CyCIF images to validate their characteristics. For instance, RCN1 typically aligned with areas known to be tumour domains, while RCN2 was more closely associated with the epidermis, thereby highlighting the structural elements within the dataset.

Segmentation of individual 3D cells with Cellpose

Individual 3D cells were segmented from the dense tissue volumes using Cellpose (https://github.com/MouseLand/cellpose),[77] a custom gradient tracking approach which aggregates x-y, y-z, x-z 2D slice cell probability and gradient maps predicted by pretrained 2D segmentation models. The full Cellpose segmentation framework, suitable for a wide range of 3D cell imaging data along with in-depth validation and determination of method applicability will be described elsewhere, see below for the Cellpost workflow specific to this project.

Image preprocessing for Cellpose

The 3D volumes were acquired at voxel resolution of 280 x 140 x 140 nm. For each 3D channel image, we resized the x-y slices by half to obtain isotropic voxels. The raw image intensity, I_{raw}^{ch} was then corrected for uneven illumination, $I_{correct}^{ch} = \overline{I_{raw}^{ch}} \frac{I_{raw}^{ch}}{I_{bg}^{ch}}$ where $\overline{I_{raw}^{ch}}$ is the mean image intensity and I_{bg}^{ch} an estimation of the background illumination obtained by downsampling the image by a factor of 8, Gaussian smoothing with sigma = 5 and resizing back to the original image dimensions. $I_{correct}^{ch}$ was then contrast-stretched to a range of 0-1, clipping any intensities less than the 2nd percentile to 0 and any greater than the 99.8th percentile to 1. Cellpose uses a single channel

cytoplasmic and nuclear signal for two-color based cell segmentation. The mean of the intensity-normalized, background-corrected HLA-AB, CD3E, CD11b, and β-actin channels was used as the cytoplasmic signal. DAPI was used as the nucleus signal. Both cytoplasmic and nucleus signals underwent a further round of background correction and contrast stretching as described above before being concatenated to form the input RGB volume image.

Running Cellpose 2D

The RGB volume was input slice-by-slice to Cellpose 2D in three different orientations; x-y, x-z, y-z to obtain three stacks of cell probability and 2D gradients. The performance of Cellpose depends on appropriate setting of the diameter parameter which relates to the size of the cells to be segmented. As the appearance of the cells may vary depending on orientation, we conduct a parameter screen with diameter = [10,100] at increments of 5 using the mid-slice for each orientation. At each diameter we compute the 'sharpness' of the predicted gradient map as the mean of the image variance evaluated over a local 5x5 pixel window in both 'x' and 'y' gradient directions. The diameter maximizing the variance after a moving average smoothing with window size of 3 was used to run Cellpose 2D on the remaining slices in the orientation. The raw cell probability output, P from Cellpose are the inputs to a sigmoid centered at zero, $1/(1+e^{-P})$.This means the probabilities vary predominantly linearly in the range -6 to +6 and this reduces the distinction between foreground and background. Thus, we clip the probabilities to the range [-88.72, 88.72] (to prevent overflow or underflow in float32) and convert back to a normalized probability value in the range 0-1 by evaluating the sigmoid, $1/(1+e^{-P})$. The probabilities from all 3 orientations are combined into one by averaging. Similarly, the 2D gradients are Gaussian smoothed with sigma=1 voxel and combined into a single 3D gradient map. Gradients are then normalized to be unit length. Lastly, we perform 3-level Otsu thresholding on the combined probability map and use the lower threshold to define the foreground binary voxels for gradient tracking.

Aggregating Cellpose 2D predictions

The volume was divided into subvolumes of (256, 512, 512) with 25% overlap. Within each subvolume we run gradient descent with momentum for 200 iterations, momenta, $\mu = 0.98$, step size $\delta = 1$ to propagate the position of foreground pixels towards its final attractor in the 3D gradient map.

$$\left(x_i^{t+1}, y_i^{t+1}, z_i^{t+1}\right) \leftarrow \left(x_i^t, y_i^t, z_i^t\right) + \frac{1}{\delta+\mu}\left(\delta \cdot \nabla\left(x_i^t, y_i^t, z_i^t\right) + \mu \cdot \nabla\left(x_i^{t-1}, y_i^{t-1}, z_i^{t-1}\right)\right)$$

Here (x_i^t, y_i^t, z_i^t) denotes the coordinate of foreground voxel i at iteration number t, μ the momentum ranging from 0-1, δ the step size and ∇ is the gradient map. Nearest neighbor interpolation is used, thus (x_i^t, y_i^t, z_i^t) is always integer valued. Gradient tracking of all subvolumes are conducted in parallel using multiprocessing. The final coordinate positions from all subvolumes are compiled. We then build a volume count map where voxels mapping to the same final coordinate adds +1 to the count. The count map is Gaussian smoothed with sigma=1 and binarized using the mean value as

the threshold. Connected component analysis identifies the unique cell as clusters where foreground voxels have been mapped to the same cell. Transferring this labelling to initial voxel positions $\left(x_i^{t=0}, y_i^{t=0}, z_i^{t=0}\right)$ generates the individual 3D cell segmentations.

Postprocessing 3D cell segmentations

Small individual cell masks (<1000 voxels^3 ≈ 20μm^3) were first removed. We also removed all cell masks that do not agree with the Cellpose predicted 3D gradient map. This is done by computing the 3D heat diffusion gradient map given the computed 3D cell segmentations and computing the mean squared error (MSE) with the input combined Cellpose 3D gradient map for each cell. Cells with MSE > 0.8 were discarded. Cells that are implausibly large, with volume greater than the mean volume $\pm$ 5 standard deviations were also discarded.

For the remainder cells, we run a label propagation[78] to enforce that each segmented cell mask comprises only a single connected component and to denoise the masks. This is done for each cell mask, M_i, by cropping a subvolume, V_i, the size of its bounding box padded isotropically by 25 voxels. Each unique cell region is represented as a positive integer label. Every label in V_i is encoded using a one-hot encoding scheme to create a binary column for each unique label. This generates a label matrix, $L_i \in \mathbb{R}^{N \times p+1}$ for V_i, where N is the total number of voxels and p the number of unique labels in V_i and one additional label for background. We then construct the affinity matrix, A, as a weighted sum ($\alpha = 0.25$) of an affinity matrix based on the intensity difference in the cytoplasmic signal between 8-connected voxel neighbors, $A_{intensity}$, and one based on the connectivity alone, $A_{laplacian}$; $A = \alpha A_{intensiy} + (1-\alpha)A_{laplacian}$. $A_{intensity} = \begin{cases} e^{-D_{intensity}/(2\mu(D_{intensity})^2)} & i \neq j \\ 1 & i = j \end{cases}$ where $D_{intensity}$ is the pairwise absolute difference matrix between two neighboring voxels i and j. $A_{laplacian} = \begin{cases} e^{-D^2_{laplacian}/(2\mu(D_{laplacian})^2)} & i \neq j \\ 1 & i = j \end{cases}$ where $D_{laplacian}$ is the graph Laplacian with a value of 1 if a voxel i is a neighbor of voxel j, and 0 otherwise. $\mu(D)$ denotes the mean value of the entries of matrix D. The iterative label propagation is

$$z \in \mathbb{R}^{N \times p}$$

$$z^{t=0} = \mathbf{0}$$

$$z^{t+1} \leftarrow (1-\gamma)A\,z^t + (\gamma)L,$$

where t is the interation number, $\mathbf{0}$, denotes the empty vector and γ is a 'clamping' factor that controls the extent the original labeling is preserved. We set $\gamma = 0.01$. We run the propagation for 25 iterations. The final z is normalized using the softmax operation and argmax is used to obtain the final labels. The refined cell mask, M_i^{refine} is defined by all voxels where z has the same cell label

i. All postprocessing steps were implemented using parallel multiprocessing iterating over individual cells.

Statistical Tests

All statistical tests were performed using MATLAB's *ttest2* implementation of the two-sample t-test without assuming equal variances and significance value of $p<0.05$.

References

1. Hickey, J. W. *et al.* Spatial mapping of protein composition and tissue organization: a primer for multiplexed antibody-based imaging. Preprint at http://arxiv.org/abs/2107.07953 (2021).

2. Slaoui, M. & Fiette, L. Histopathology procedures: from tissue sampling to histopathological evaluation. *Methods Mol Biol* **691**, 69–82 (2011).

3. Prasad, A. & Alizadeh, E. Cell Form and Function: Interpreting and Controlling the Shape of Adherent Cells. *Trends Biotechnol* **37**, 347–357 (2019).

4. Lin, J.-R. *et al.* Highly multiplexed immunofluorescence imaging of human tissues and tumors using t-CyCIF and conventional optical microscopes. *eLife* **7**, (2018).

5. Clark, W. H. *et al.* A study of tumor progression: The precursor lesions of superficial spreading and nodular melanoma. *Human Pathology* **15**, 1147–1165 (1984).

6. Gaglia, G. *et al.* Lymphocyte networks are dynamic cellular communities in the immunoregulatory landscape of lung adenocarcinoma. *Cancer Cell* **41**, 871-886.e10 (2023).

7. Kapałczyńska, M. *et al.* 2D and 3D cell cultures - a comparison of different types of cancer cell cultures. *Arch Med Sci* **14**, 910–919 (2018).

8. Rao, A., Barkley, D., França, G. S. & Yanai, I. Exploring tissue architecture using spatial transcriptomics. *Nature* **596**, 211–220 (2021).

9. Herman, B. & Lemasters, J. J. *Optical Microscopy: Emerging Methods and Applications*. (Elsevier, 2012).

10. Du, Z. *et al.* Qualifying antibodies for image-based immune profiling and multiplexed tissue imaging. *Nat Protoc* **14**, 2900–2930 (2019).

11. Wu, Y., Pegoraro, A. F., Weitz, D. A., Janmey, P. & Sun, S. X. The correlation between cell and nucleus size is explained by an eukaryotic cell growth model. *PLoS Comput Biol* **18**, e1009400 (2022).

12. Benvenuti, F. *et al.* Requirement of Rac1 and Rac2 Expression by Mature Dendritic Cells for T Cell Priming. *Science* **305**, 1150–1153 (2004).

13. Blauth, E., Kubitschke, H., Gottheil, P., Grosser, S. & Käs, J. A. Jamming in Embryogenesis and Cancer Progression. *Frontiers in Physics* **9**, (2021).

14. Chen, H., Li, D. & Bar-Joseph, Z. SCS: cell segmentation for high-resolution spatial transcriptomics. *Nat Methods* **20**, 1237–1243 (2023).

15. Sehgal, P. B. *et al.* Murine GFP-Mx1 forms nuclear condensates and associates with cytoplasmic intermediate filaments: Novel antiviral activity against VSV. *J Biol Chem* **295**, 18023–18035 (2021).

16. Woo, S.-R. *et al.* Differential subcellular localization of the regulatory T-cell protein LAG-3 and the coreceptor CD4. *Eur J Immunol* **40**, 1768–1777 (2010).

17. Lin, L. *et al.* Granzyme B secretion by human memory CD4 T cells is less strictly regulated compared to memory CD8 T cells. *BMC Immunol* **15**, 36 (2014).

18. Nirmal, A. J. *et al.* The Spatial Landscape of Progression and Immunoediting in Primary Melanoma at Single-Cell Resolution. *Cancer Discovery* **12**, 1518–1541 (2022).

19. Muller, W. A. Getting Leukocytes to the Site of Inflammation. *Vet Pathol* **50**, 7–22 (2013).

20. Van Goethem, E., Poincloux, R., Gauffre, F., Maridonneau-Parini, I. & Le Cabec, V. Matrix Architecture Dictates Three-Dimensional Migration Modes of Human Macrophages: Differential Involvement of Proteases and Podosome-Like Structures. *The Journal of Immunology* **184**, 1049–1061 (2010).

21. Kuczek, D. E. *et al.* Collagen density regulates the activity of tumor-infiltrating T cells. *j. immunotherapy cancer* **7**, 68 (2019).

22. Willsmore, Z. N. *et al.* B Cells in Patients With Melanoma: Implications for Treatment With Checkpoint Inhibitor Antibodies. *Front Immunol* **11**, 622442 (2021).

23. Yamaguchi, H. & Condeelis, J. Regulation of the actin cytoskeleton in cancer cell migration and invasion. *Biochimica et Biophysica Acta (BBA) - Molecular Cell Research* **1773**, 642–652 (2007).

24. Caridi, C. P., Plessner, M., Grosse, R. & Chiolo, I. Nuclear actin filaments in DNA repair dynamics. *Nat Cell Biol* **21**, 1068–1077 (2019).

25. Rickelt, S. *et al.* Subtypes of melanocytes and melanoma cells distinguished by their intercellular contacts: heterotypic adherens junctions, adhesive associations, and dispersed desmoglein 2 glycoproteins. *Cell Tissue Res* **334**, 401–422 (2008).

26. Foty, R. A. & Steinberg, M. S. The differential adhesion hypothesis: a direct evaluation. *Dev Biol* **278**, 255–263 (2005).

27. Wu, Y. & Zhou, B. P. Inflammation: a driving force speeds cancer metastasis. *Cell Cycle* **8**, 3267–3273 (2009).

28. Hodis, E. *et al.* A Landscape of Driver Mutations in Melanoma. *Cell* **150**, 251–263 (2012).

29. Jackett, L. A. & Scolyer, R. A. A Review of Key Biological and Molecular Events Underpinning Transformation of Melanocytes to Primary and Metastatic Melanoma. *Cancers (Basel)* **11**, 2041 (2019).

30. Lian, C. G. *et al.* LOSS OF 5-HYDROXYMETHYLCYTOSINE IS AN EPIGENETIC HALLMARK OF MELANOMA. *Cell* **150**, 1135–1146 (2012).

31. Smoller, B. R. Histologic criteria for diagnosing primary cutaneous malignant melanoma. *Mod Pathol* **19**, S34–S40 (2006).

32. Lezcano, C., Jungbluth, A. A., Nehal, K. S., Hollmann, T. J. & Busam, K. J. PRAME Expression in Melanocytic Tumors. *Am J Surg Pathol* **42**, 1456–1465 (2018).

33. Chudnovsky, Y., Khavari, P. A. & Adams, A. E. Melanoma genetics and the development of rational therapeutics. *J Clin Invest* **115**, 813–824 (2005).

34. Kaufmann, C. *et al.* The role of cyclin D1 and Ki-67 in the development and prognostication of thin melanoma. *Histopathology* **77**, 460–470 (2020).

35. Fetsch, P. A. *et al.* Melanoma-associated antigen recognized by T cells (MART-1): the advent of a preferred immunocytochemical antibody for the diagnosis of metastatic malignant melanoma with fine-needle aspiration. *Cancer* **87**, 37–42 (1999).

36. Boiko, A. D. *et al.* Human melanoma-initiating cells express neural crest nerve growth factor receptor CD271. *Nature* **466**, 133–137 (2010).

37. Kim, Y. J. *et al.* Melanoma dedifferentiation induced by IFN-γ epigenetic remodeling in response to anti-PD-1 therapy. *J Clin Invest* **131**, e145859, 145859 (2021).

38. Watanabe, R. *et al.* Human skin is protected by four functionally and phenotypically discrete populations of resident and recirculating memory T cells. *Sci Transl Med* **7**, 279ra39 (2015).

39. Utzschneider, D. T. *et al.* Early precursor T cells establish and propagate T cell exhaustion in chronic infection. *Nat Immunol* **21**, 1256–1266 (2020).

40. Burger, M. L. *et al.* Antigen dominance hierarchies shape TCF1+ progenitor CD8 T cell phenotypes in tumors. *Cell* **184**, 4996-5014.e26 (2021).

41. Miller, B. C. *et al.* Subsets of exhausted CD8+ T cells differentially mediate tumor control and respond to checkpoint blockade. *Nat Immunol* **20**, 326–336 (2019).

42. Kallies, A., Zehn, D. & Utzschneider, D. T. Precursor exhausted T cells: key to successful immunotherapy? *Nat Rev Immunol* **20**, 128–136 (2020).

43. Escobar, G., Mangani, D. & Anderson, A. C. T cell factor 1 (Tcf1): a master regulator of the T cell response in disease. *Sci Immunol* **5**, eabb9726 (2020).

44. Dustin, M. L. The immunological synapse. *Cancer Immunol Res* **2**, 1023–1033 (2014).

45. Cabrita, R. *et al.* Tertiary lymphoid structures improve immunotherapy and survival in melanoma. *Nature* **577**, 561–565 (2020).

46. Huang, F., Santinon, F., Flores González, R. E. & del Rincón, S. V. Melanoma Plasticity: Promoter of Metastasis and Resistance to Therapy. *Front Oncol* **11**, 756001 (2021).

47. Oyler-Yaniv, A. *et al.* A Tunable Diffusion-Consumption Mechanism of Cytokine Propagation Enables Plasticity in Cell-to-Cell Communication in the Immune System. *Immunity* **46**, 609–620 (2017).

48. Kiemen, A. *et al.* CODA: Quantitative 3D reconstruction of large tissues at cellular resolution. *Nat Methods* **19**, 1490–1499 (2022).

49. Lin, J.-R. *et al.* Multiplexed 3D atlas of state transitions and immune interaction in colorectal cancer. *Cell* **186**, 363-381.e19 (2023).

50. Stelzer, E. H. K. *et al.* Light sheet fluorescence microscopy. *Nat Rev Methods Primers* **1**, 1–25 (2021).

51. Keller, M. S. *et al.* Vitessce: integrative visualization of multimodal and spatially-resolved single-cell data. Preprint at https://doi.org/10.31219/osf.io/y8thv (2021).

52. Manz, T. *et al.* Viv: multiscale visualization of high-resolution multiplexed bioimaging data on the web. *Nat Methods* **19**, 515–516 (2022).

53. Wallace, W., Schaefer, L. H. & Swedlow, J. R. A Workingperson's Guide to Deconvolution in Light Microscopy. *BioTechniques* **31**, 1076–1097 (2001).

54. Fish, K. N. Total Internal Reflection Fluorescence (TIRF) Microscopy. *CP Cytometry* **50**, (2009).

55. Axelrod, D., Thompson, N. L. & Burghardt, T. P. Total internal reflection fluorescent microscopy. *Journal of Microscopy* **129**, 19–28 (1983).

56. Egger, M. D. & Petráň, M. New Reflected-Light Microscope for Viewing Unstained Brain and Ganglion Cells. *Science* **157**, 305–307 (1967).

57. Wilson, T. Resolution and optical sectioning in the confocal microscope: PROPERTIES OF THE FLUORESCENT CONFOCAL MICROSCOPE. *Journal of Microscopy* **244**, 113–121 (2011).

58. Wilson, T. Optical sectioning in confocal fluorescent microscopes. *Journal of Microscopy* **154**, 143–156 (1989).

59. Murray, J. M., Appleton, P. L., Swedlow, J. R. & Waters, J. C. Evaluating performance in three-dimensional fluorescence microscopy. *J Microsc* **228**, 390–405 (2007).

60. Denk, W., Strickler, J. H. & Webb, W. W. Two-Photon Laser Scanning Fluorescence Microscopy. *Science* **248**, 73–76 (1990).

61. Campagnola, P. J. *et al.* Three-Dimensional High-Resolution Second-Harmonic Generation Imaging of Endogenous Structural Proteins in Biological Tissues. *Biophysical Journal* **82**, 493–508 (2002).

62. Campagnola, P. J., Wei, M., Lewis, A. & Loew, L. M. High-Resolution Nonlinear Optical Imaging of Live Cells by Second Harmonic Generation. *Biophysical Journal* **77**, 3341–3349 (1999).

63. Zipfel, W. R. *et al.* Live tissue intrinsic emission microscopy using multiphoton-excited native fluorescence and second harmonic generation. *Proc. Natl. Acad. Sci. U.S.A.* **100**, 7075–7080 (2003).

64. Ghose, S. *et al. Human Digital Twin: Automated Cell Type Distance Computation and 3D Atlas Construction in Multiplexed Skin Biopsies*. http://biorxiv.org/lookup/doi/10.1101/2022.03.30.486438 (2022) doi:10.1101/2022.03.30.486438.

65. Kuett, L. *et al.* Three-dimensional imaging mass cytometry for highly multiplexed molecular and cellular mapping of tissues and the tumor microenvironment. *Nat Cancer* **3**, 122–133 (2022).

66. Ghose, S. *et al.* 3D reconstruction of skin and spatial mapping of immune cell density, vascular distance and effects of sun exposure and aging. *Commun Biol* **6**, 718 (2023).

67. Renier, N. *et al.* iDISCO: A Simple, Rapid Method to Immunolabel Large Tissue Samples for Volume Imaging. *Cell* **159**, 896–910 (2014).

68. Tomer, R., Ye, L., Hsueh, B. & Deisseroth, K. Advanced CLARITY for rapid and high-resolution imaging of intact tissues. *Nat Protoc* **9**, 1682–1697 (2014).

69. Tanaka, N. *et al.* Whole-tissue biopsy phenotyping of three-dimensional tumours reveals patterns of cancer heterogeneity. *Nat Biomed Eng* **1**, 796–806 (2017).

70. Murray, E. *et al.* Simple, Scalable Proteomic Imaging for High-Dimensional Profiling of Intact Systems. *Cell* **163**, 1500–1514 (2015).

71. Chen, B.-C. *et al.* Lattice light-sheet microscopy: Imaging molecules to embryos at high spatiotemporal resolution. *Science* **346**, 1257998 (2014).

72. Dean, K. M., Roudot, P., Welf, E. S., Danuser, G. & Fiolka, R. Deconvolution-free Subcellular Imaging with Axially Swept Light Sheet Microscopy. *Biophysical Journal* **108**, 2807–2815 (2015).

73. Scholaert, M. *et al. 3-D Deconvolution of Human Skin Immune Architecture with Multiplex Annotated Tissue Imaging System (MANTIS)*. http://biorxiv.org/lookup/doi/10.1101/2023.01.13.523748 (2023) doi:10.1101/2023.01.13.523748.

74. Van Ineveld, R. L. *et al.* Revealing the spatio-phenotypic patterning of cells in healthy and tumor tissues with mLSR-3D and STAPL-3D. *Nat Biotechnol* **39**, 1239–1245 (2021).

75. Shi, L., Wei, M. & Min, W. Highly-Multiplexed Tissue Imaging with Raman Dyes. *JoVE* 63547 (2022) doi:10.3791/63547.

76. Lin, J.-R. *et al.* Highly multiplexed immunofluorescence imaging of human tissues and tumors using t-CyCIF and conventional optical microscopes. *eLife* **7**, e31657 (2018).

77. Stringer, C., Wang, T., Michaelos, M. & Pachitariu, M. Cellpose: a generalist algorithm for cellular segmentation. *Nat Methods* **18**, 100–106 (2021).

78. Zhou, D., Bousquet, O., Lal, T., Weston, J. & Schölkopf, B. Learning with Local and Global Consistency. in *Advances in Neural Information Processing Systems* (eds. Thrun, S., Saul, L. & Schölkopf, B.) vol. 16 (MIT Press, 2003).

Figure 1

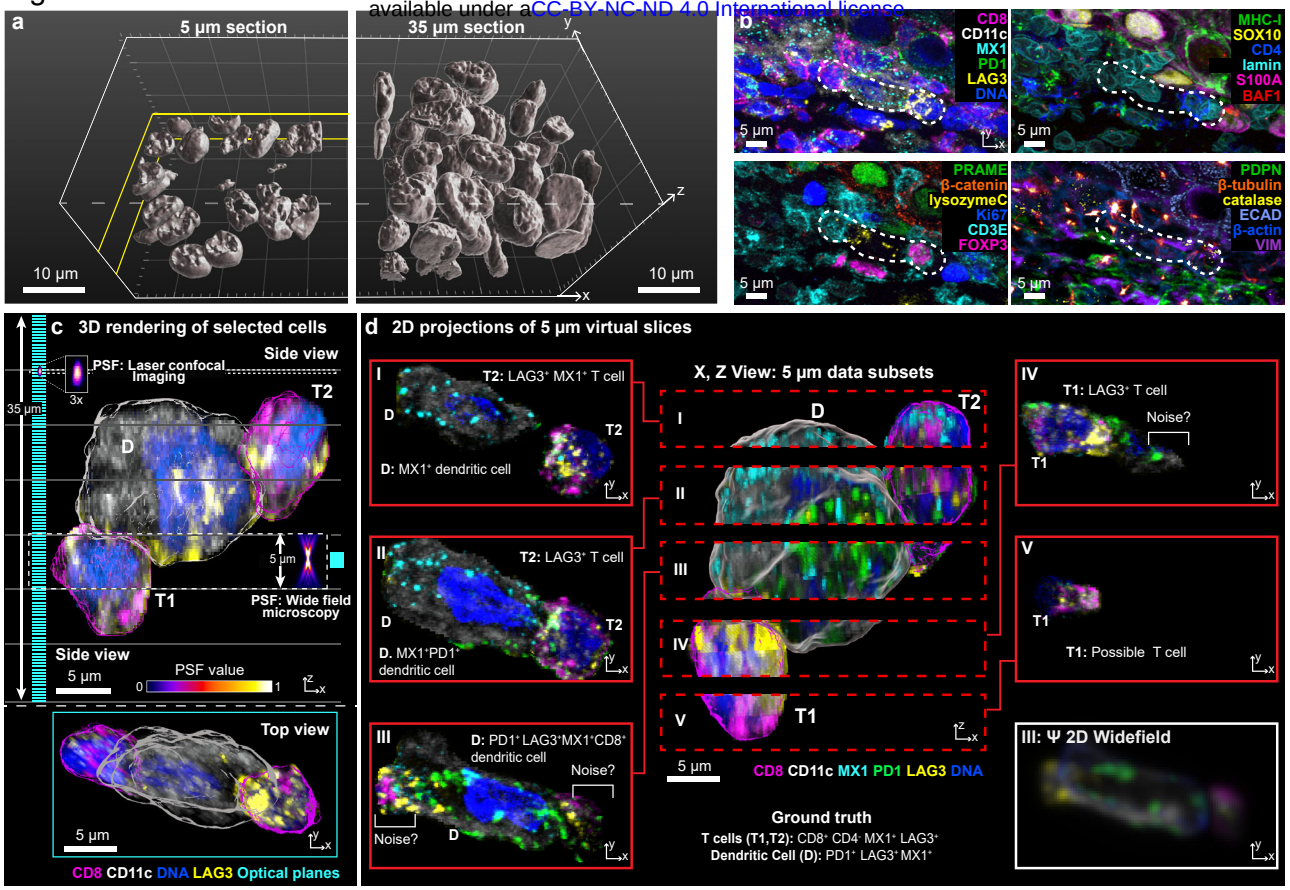

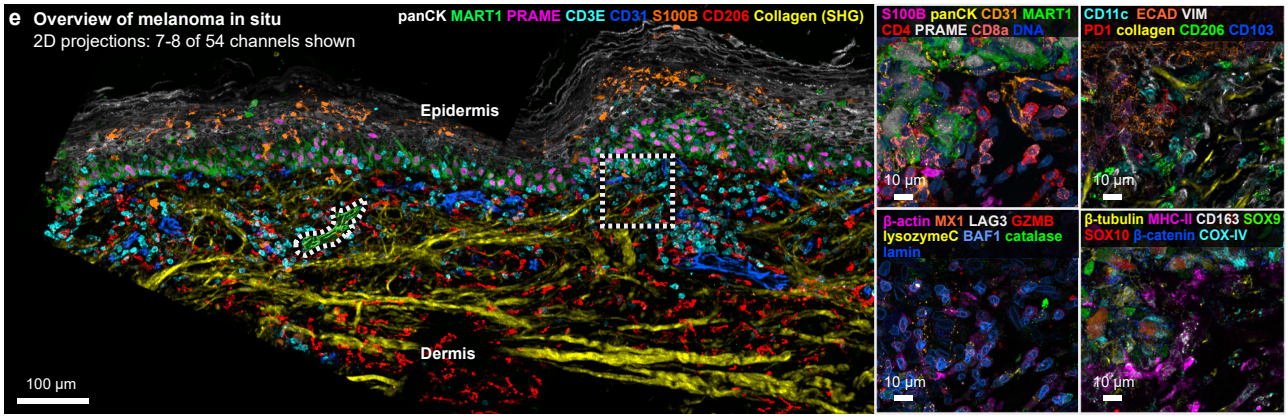

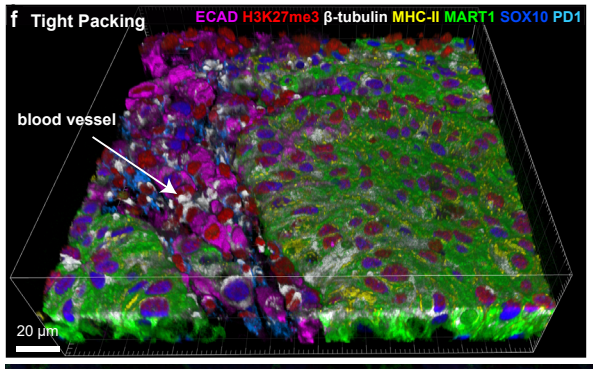

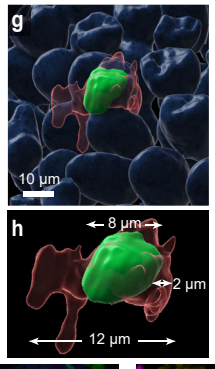

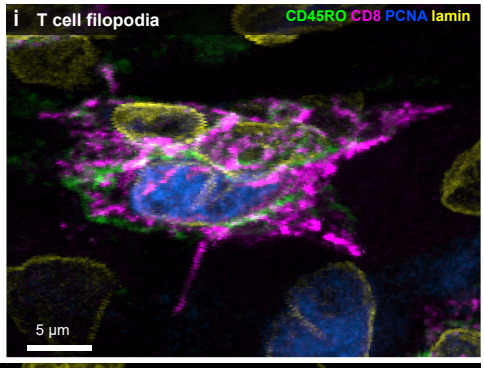

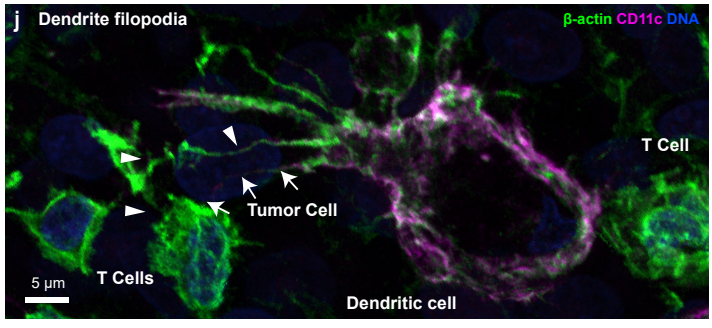

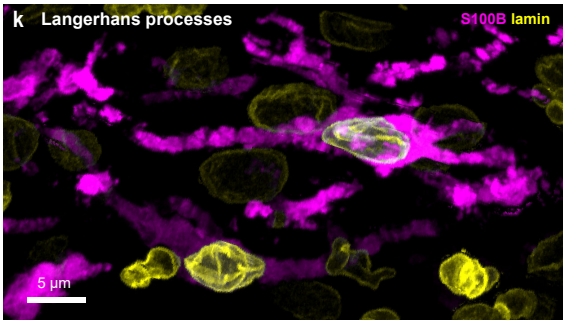

Figure 2

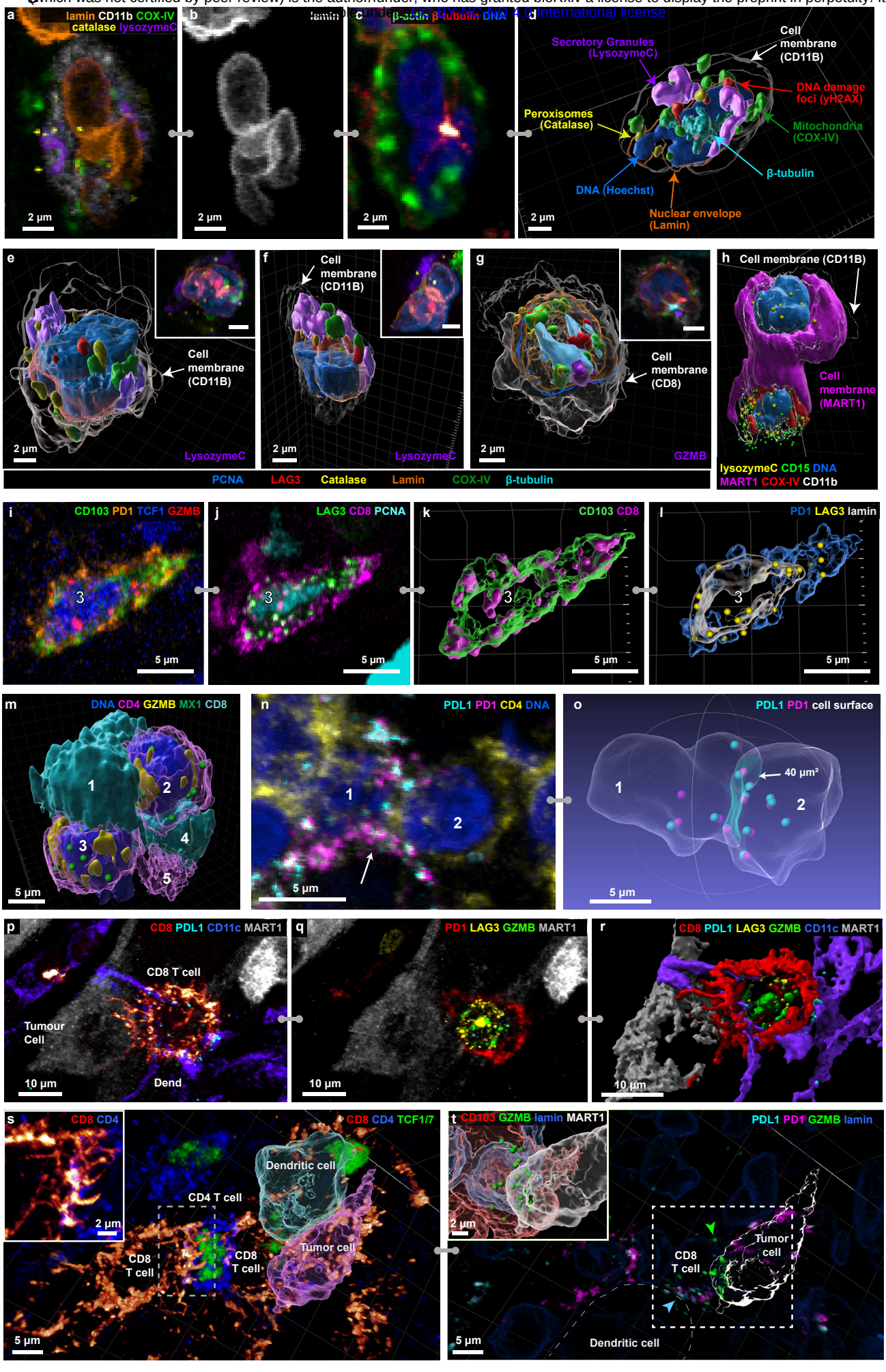

Figure 3

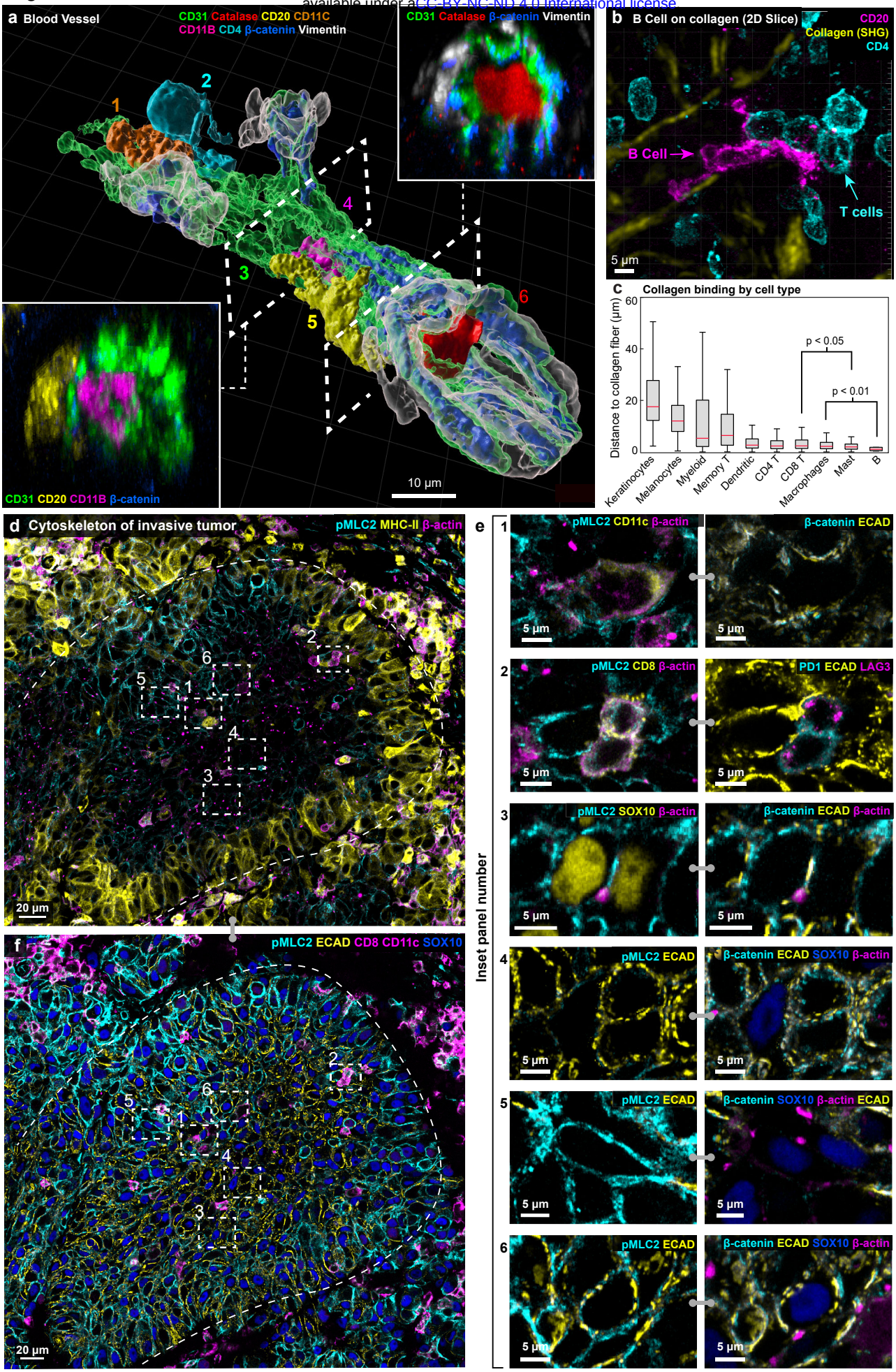

Figure 4

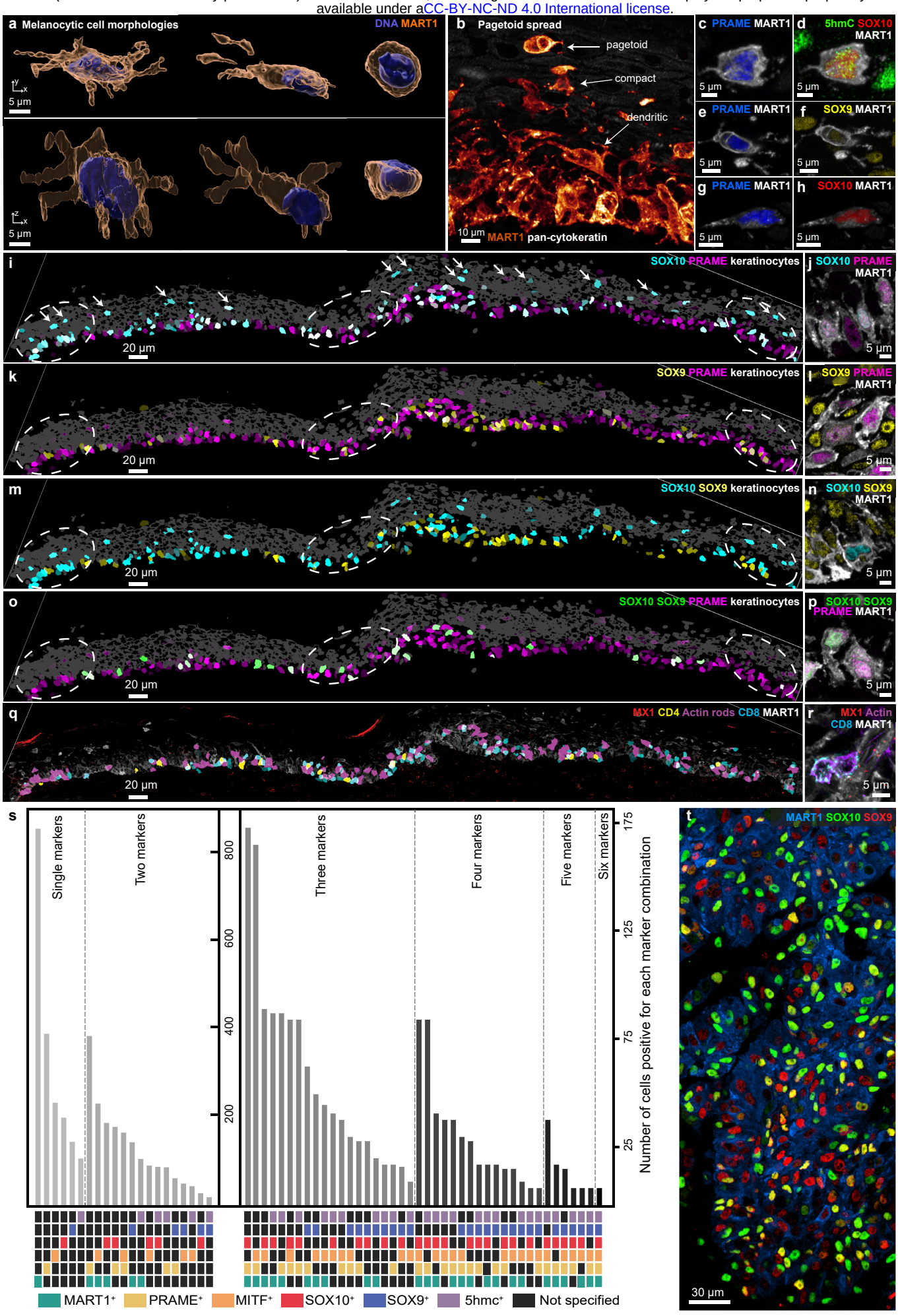

Figure 5

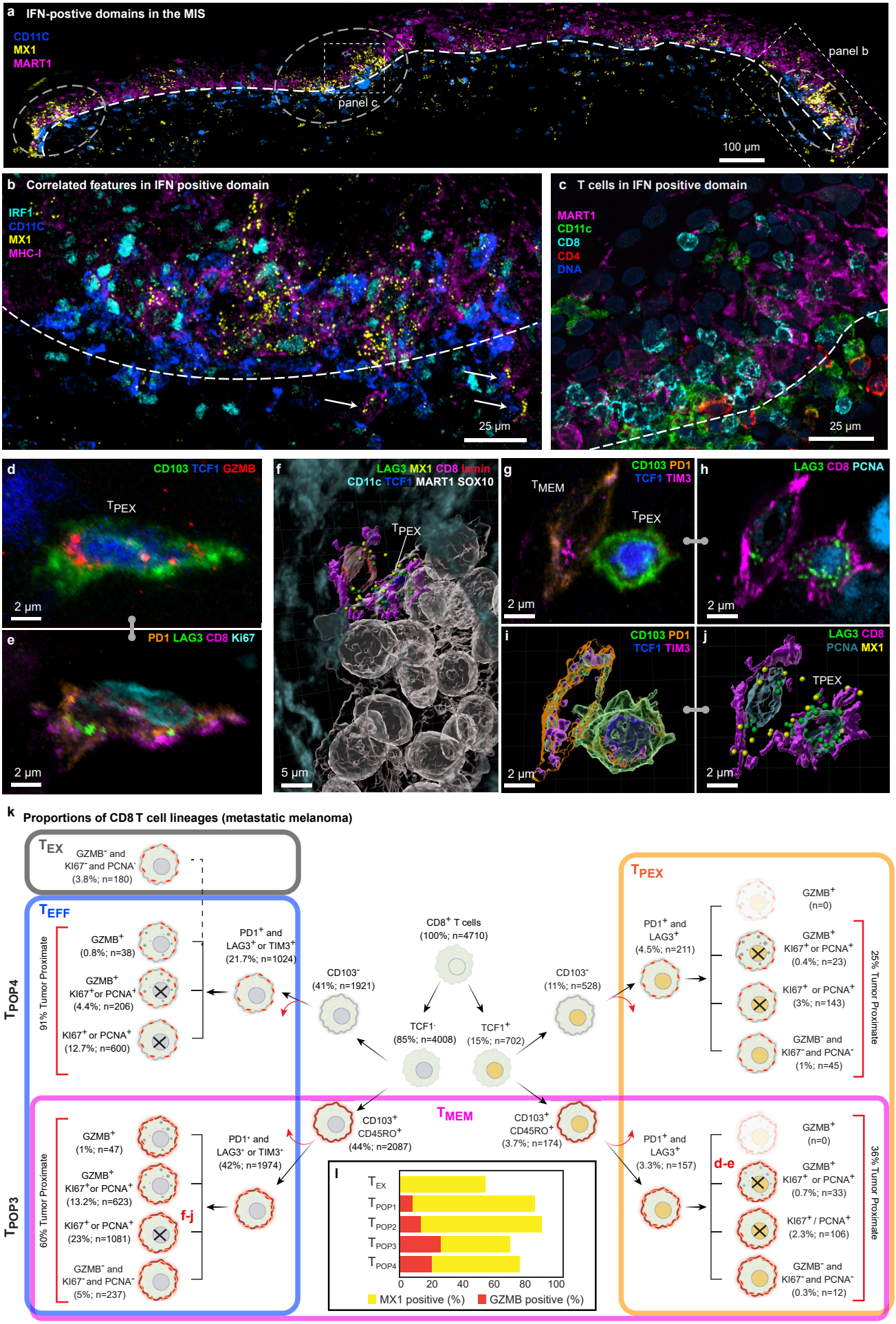

Figure 6

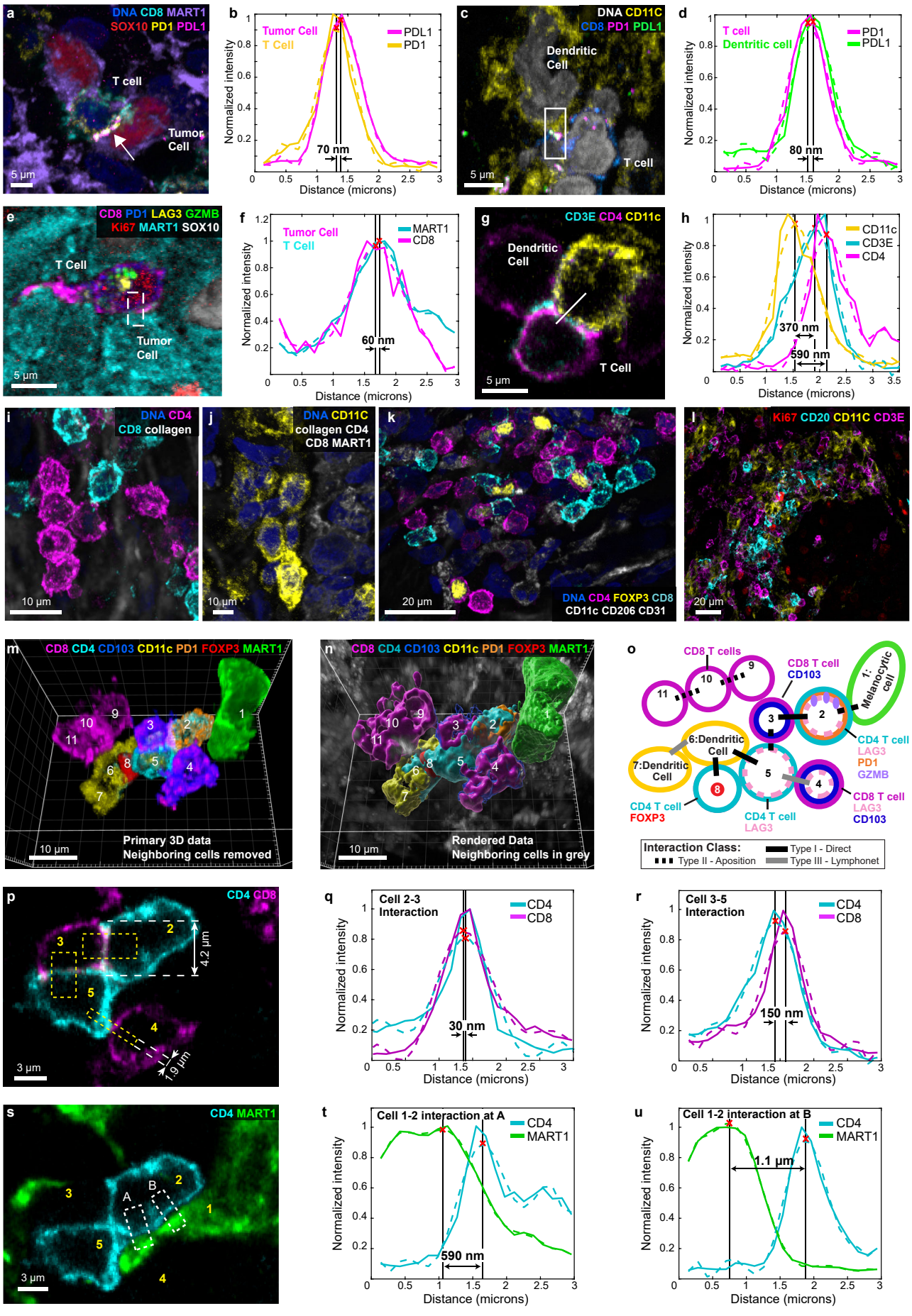

Extended Data Figure 1

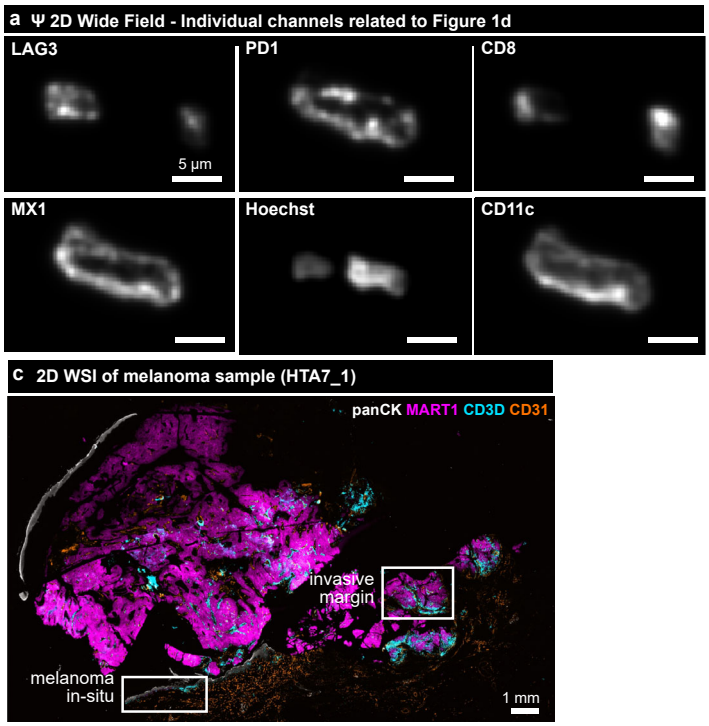

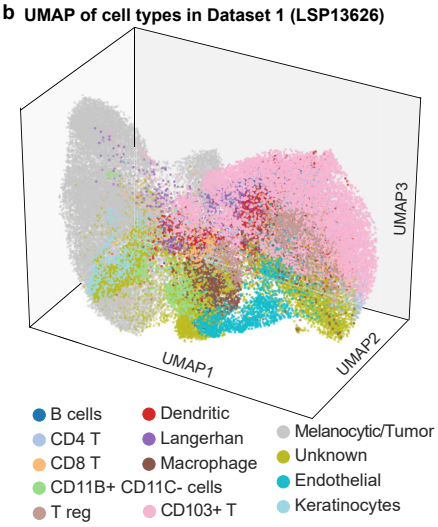

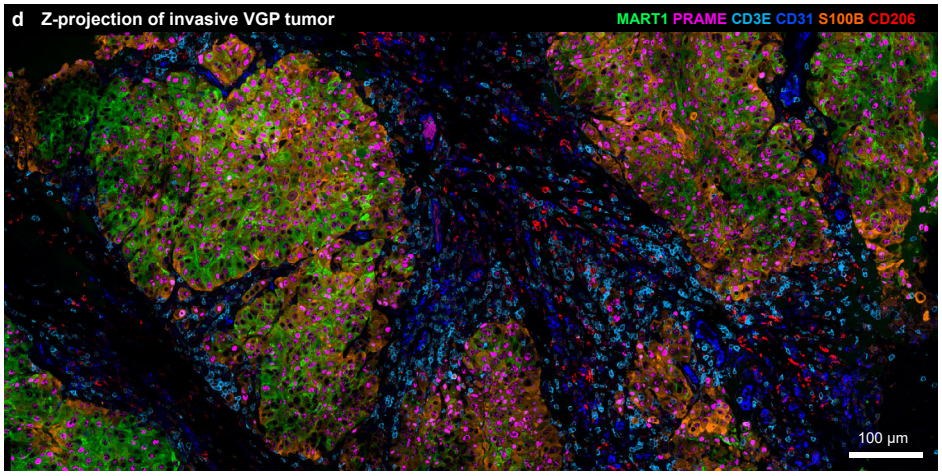

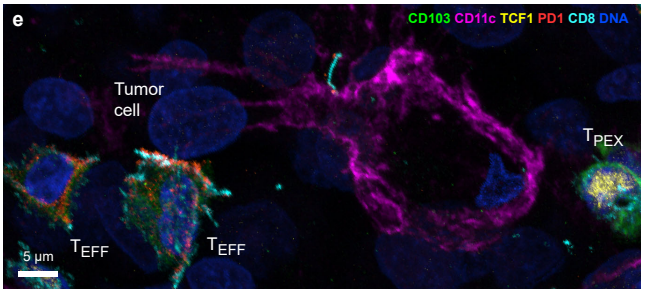

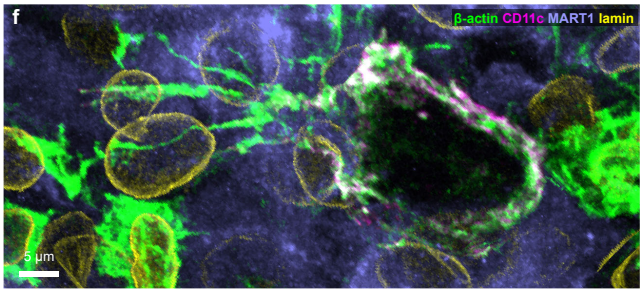

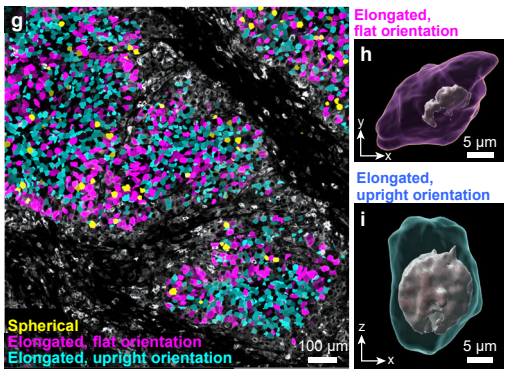

Extended Data Figure 2

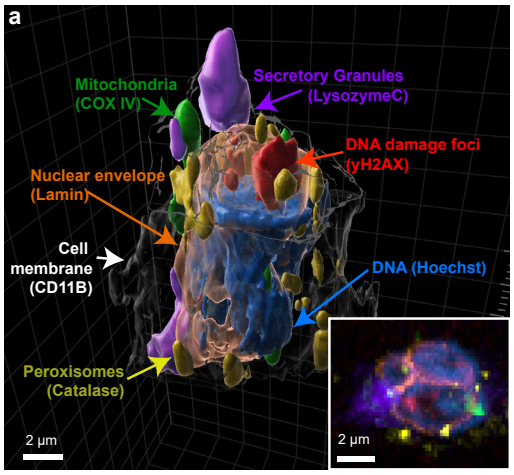

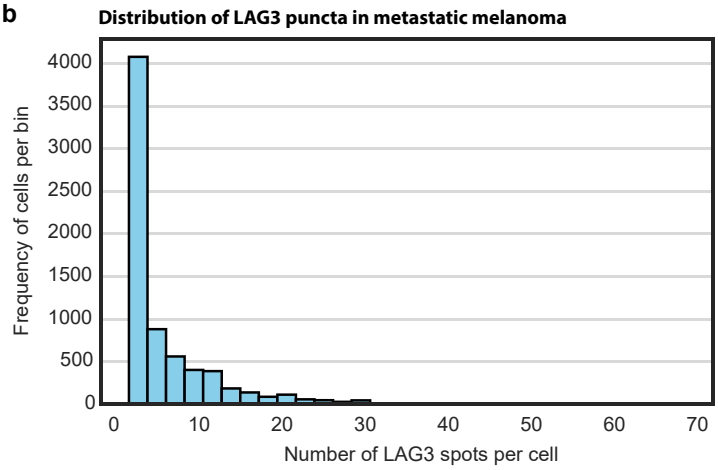

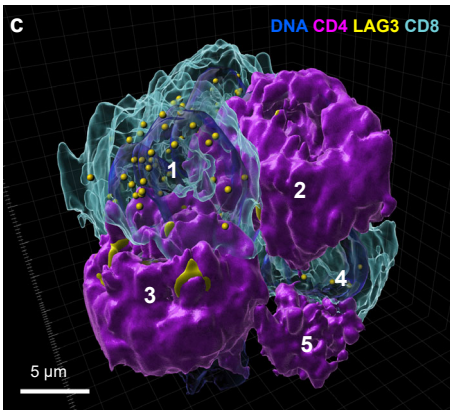

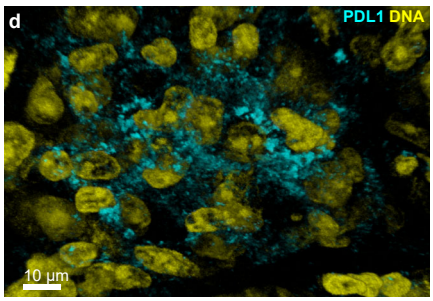

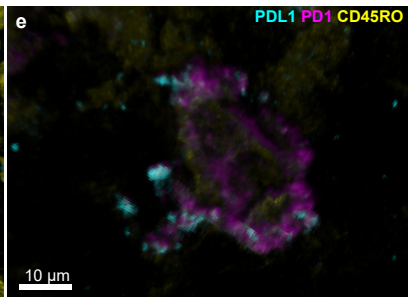

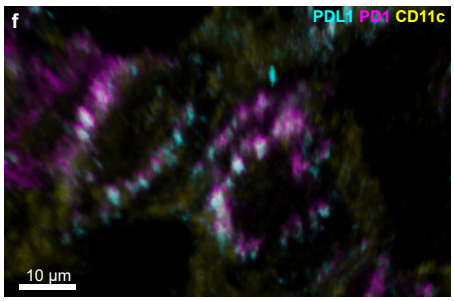

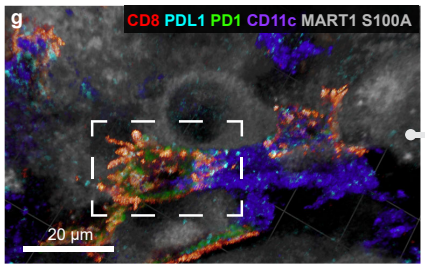

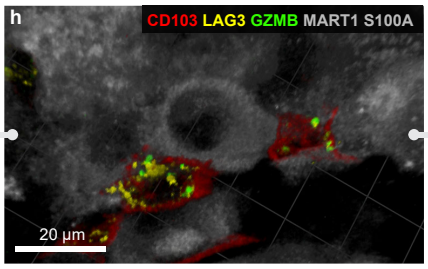

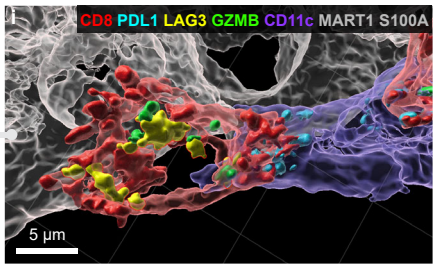

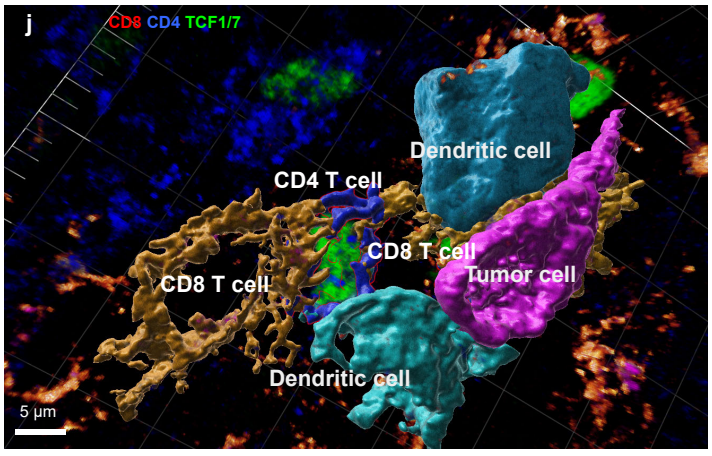

Extended Data Figure 3

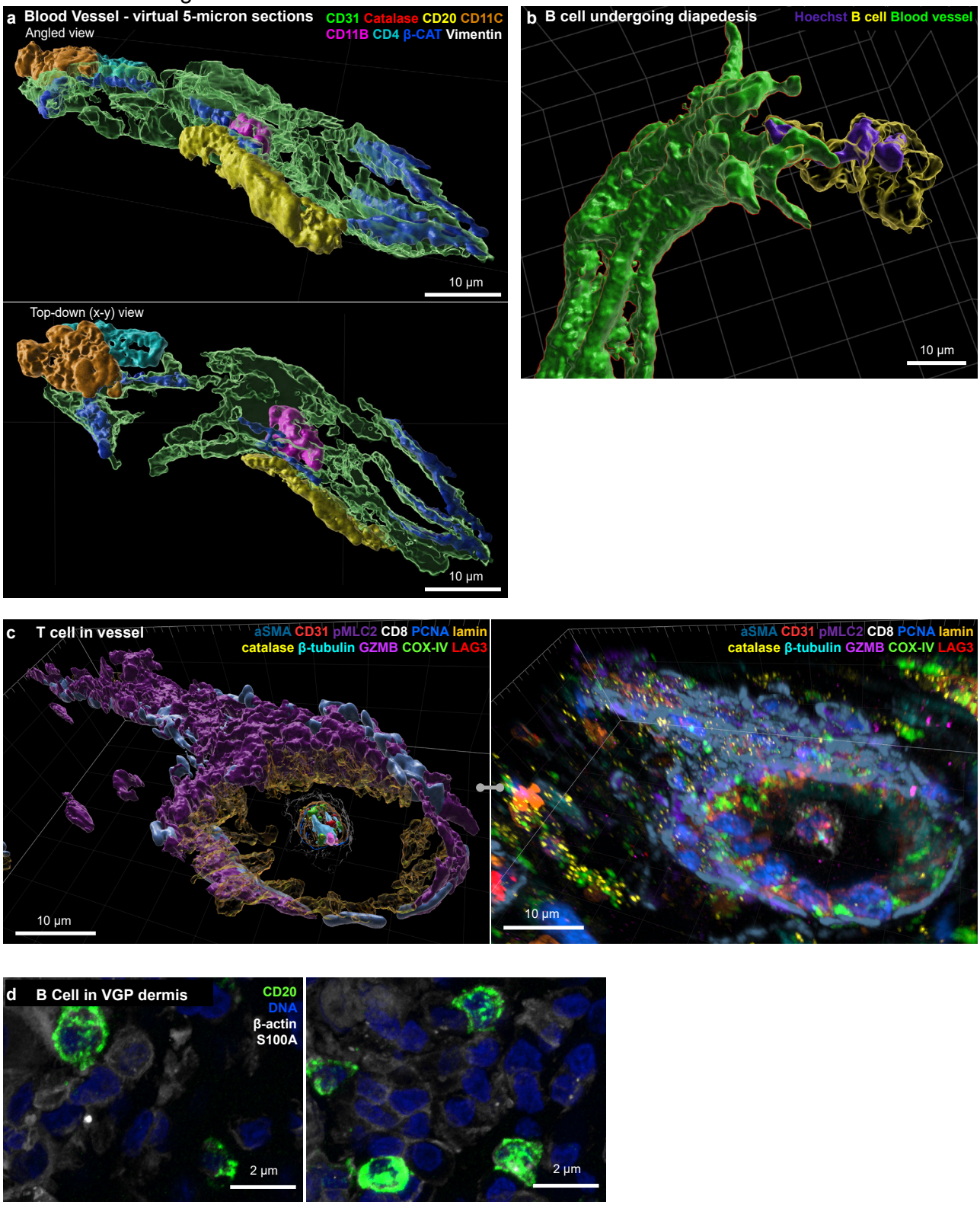

Extended Data Figure 4

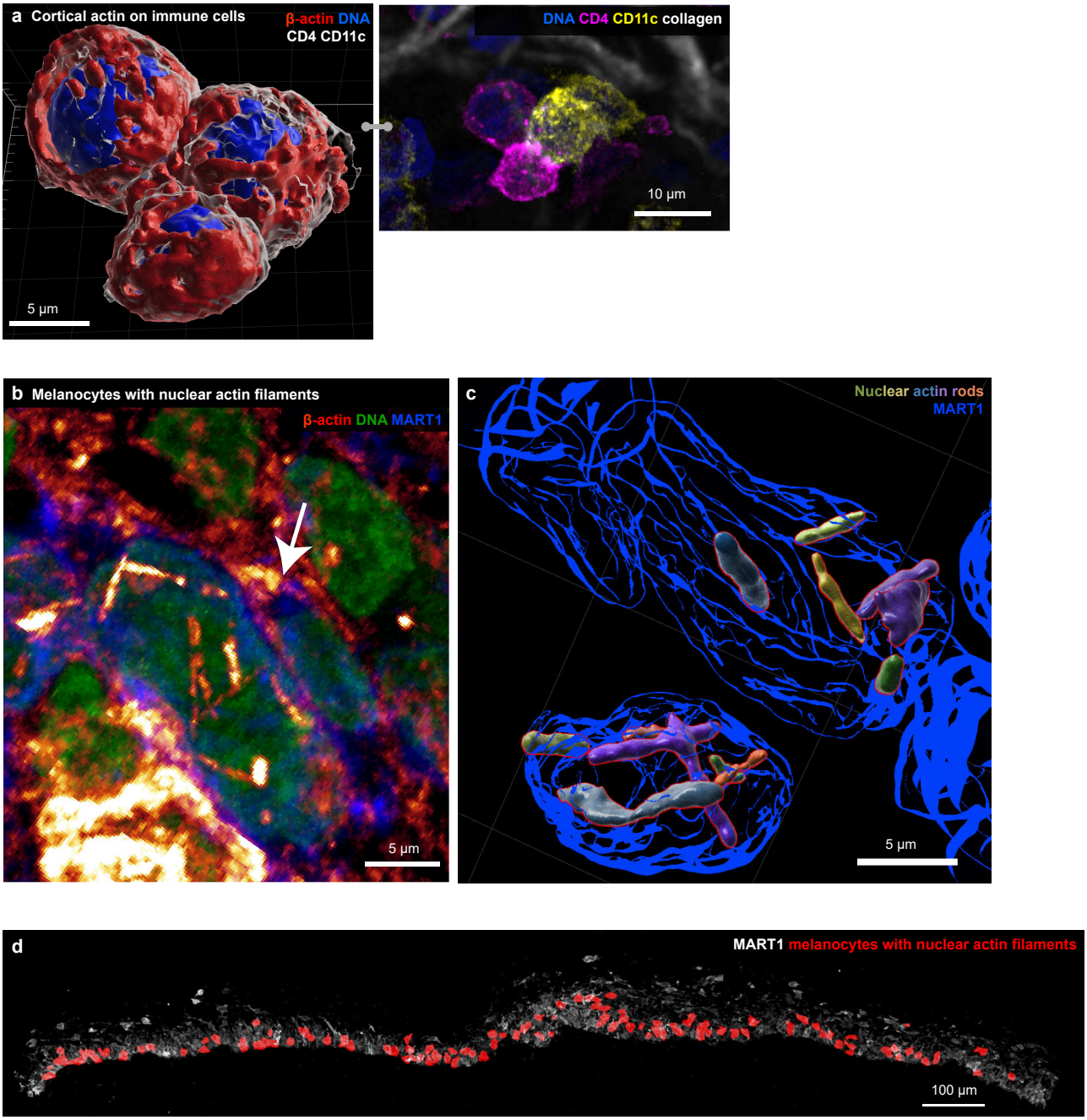

Extended Data Figure 5

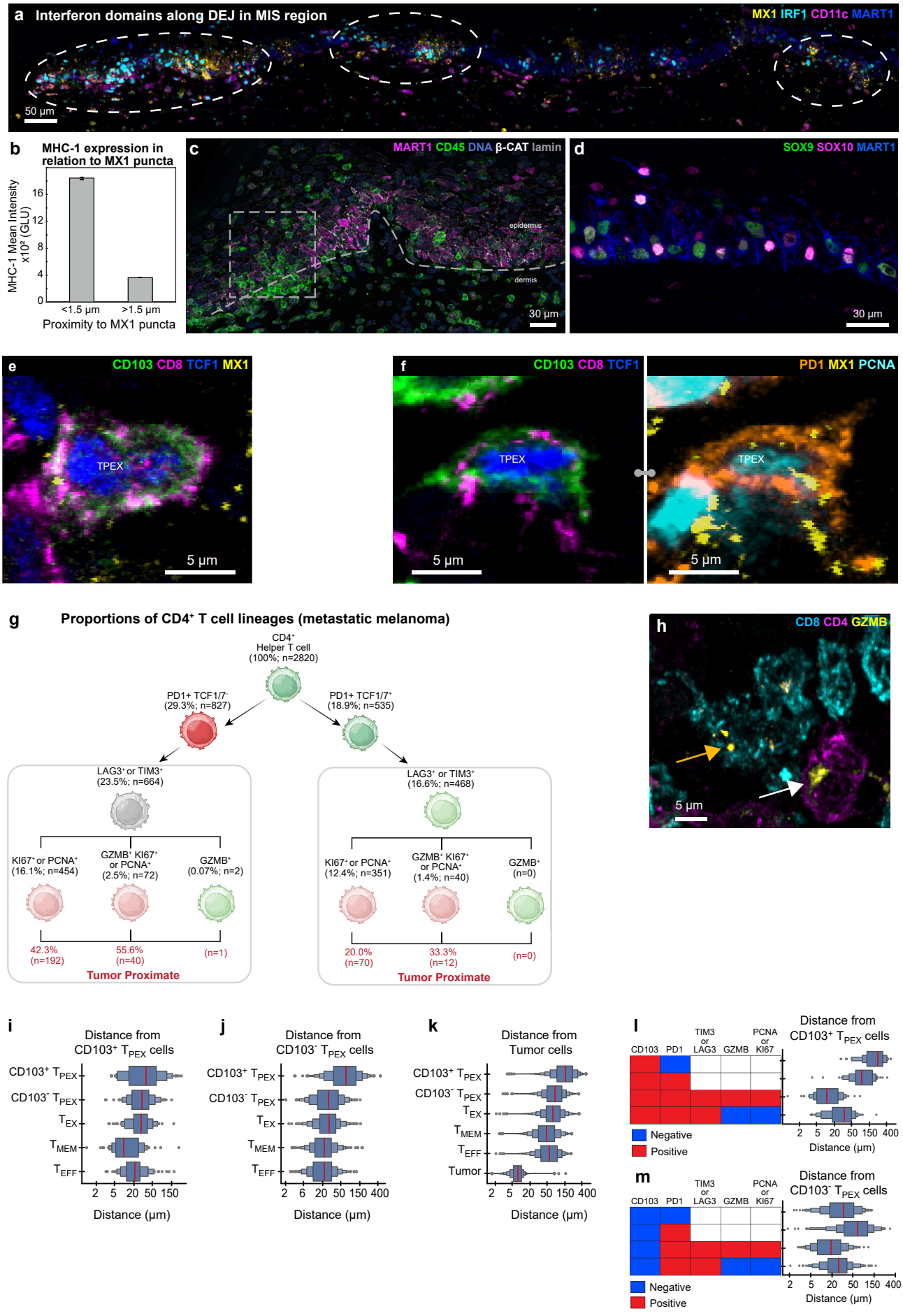

Extended Data Figure 6

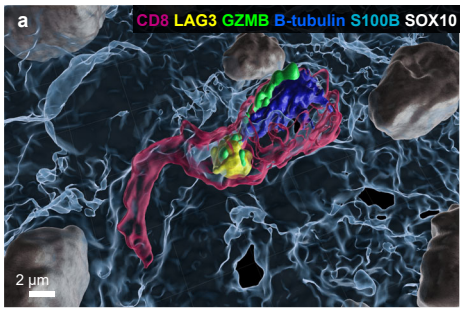

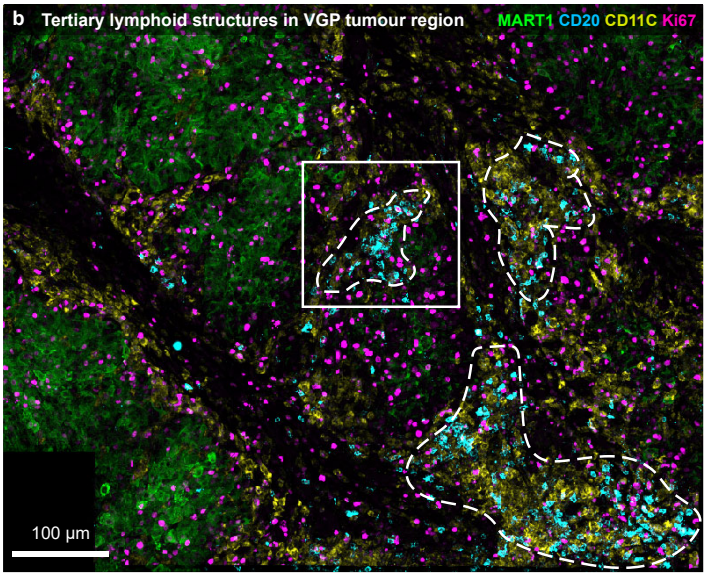

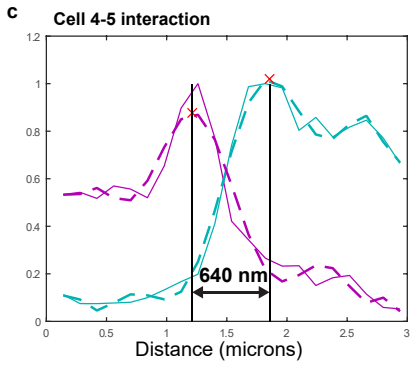

Extended Data Figure 7